Transition Metal Gettering Studies and Simulation for the Optimization of Silicon Photovoltaic Device Processing

by

Aimée Louise Smith

Submitted to the Department of Materials Science and Engineering
in partial fulfillment of the requirements for the degree of

Doctor of Philosophy

at the

MASSACHUSETTS INSTITUTE OF TECHNOLOGY

May 2002

Author ....
Department of Materials Science and Engineering
May 10, 2002

Certified by ....
Lionel C. Kimerling
Thomas Lord Professor of Materials Science and Engineering
Thesis Supervisor

Accepted by ....
Harry Louis Tuller
Chairman, Department Committee on Graduate Students

Transition Metal Gettering Studies and Simulation for the Optimization of Silicon Photovoltaic Device Processing

by

Aimée Louise Smith

Submitted to the Department of Materials Science and Engineering
on May 10, 2002, in partial fulfillment of the
requirements for the degree of
Doctor of Philosophy

Abstract

We use what is known about transition metal (TM) defect thermodynamic driving forces and kinetic responses to make predictive simulation of gettering during solar cell fabrication possible. We have developed a simulator to explore the impact of various device and process parameters on gettering effectiveness. The relevant heat treatments are ramps up in temperature, isothermal annealing, and cools from high temperature down to room temperature. We explore a range of surface conditions, density and size of heterogeneous nucleation sites in the bulk, and the degree of contamination in order to create a framework in which to examine these mechanisms acting in concert. Such simulations enable process optimization for gettering. For solar cell processing, segregation to an Al back contact layer is routine. We have estimated the segregation coefficient between a p-type Si wafer and a molten Al layer by the Calphad method and use these results to estimate the thermodynamic driving force for redistribution of Fe into the Al layer.

We simulate gettering treatments of supersaturated levels of Fe contamination in Si samples with $FeSi_2$ and Al contacts and compare these results with data at various temperatures. The gettering data for $FeSi_2$ contacts follow a simple exponential decay and can be simulated with appropriate choice of internal gettering time constant. We recognize that radiative heating dominates the temperature ramp for samples in evacuated quartz ampoules and use reasonable parameters to include this effect in our simulations. Fitting parameters for [Fe] data taken from heat treatments at 755°C on samples with $FeSi_2$ and Al contacts successfully predict the gettering data of Al coated samples treated at 810°C. Discrepencies in the data for Al coated samples treated at 695°C and data for Al coated samples treated at 755°C after long times have exposed a new mechanism dominating internal gettering processes. We propose the existence of a silicide precipitate growth retardation mechanism as a result of supersaturation of the Si vacancy (V). Accumulation of V reduces the ability of precipitates to relax strain free-energy (Δg_{strain}) by further V emission.

We performed Cu gettering experiments on p/p^+ epitaxial wafers. Photoluminescence measurements revealed significant Cu removal from the epitaxial region com-

pared to similarly doped uniformly doped float zone (FZ) Si wafers. Step etching revealed haze, indicating the presence of silicide precipitates below the epitaxial layer in the heavily doped substrates. Uncontaminated heat treated epitaxial wafers did not demonstrate the presence of haze after step etching. This finding demonstrates that redistribution of Cu from the lightly doped expitaxial layer to the heavily doped substrate as predicted by the dopant enhanced solubility model has occurred.

The commonly used $T^{3/2}$ model for effective density of conduction and valence band states (N_C and N_V respectively) is not accurate for Si, even in the device operation regime, and the available experimentally determined relations of Green do not extend past 500K. We have constructed a DOS model using *ab initio* calculations and temperature appropriate Fermi-Dirac statistics to generate an extrapolation of DOS into the processing temperature regime. The available data of dopant enhanced solubility of Fe in Si can be modeled within error assuming the Fe defect level (E_T) remains at a constant fraction of the energy gap (E_G) by either the $T^{3/2}$ model for N_C and N_V or our *ab initio* DOS model. While a more quantitative understanding of Si in the processing temperature regime is needed, there is no compelling evidence at this time for the instability of E_T contrary to what has been proposed in the literature.

We apply the metallurgical construct of the time-temperature-transformation (TTT) diagram to the system of gettering in Si device processing. We use the gettering simulator to generate TTT gettering design diagrams. Because of the large number of wafer parameters and the interactions of these with time, temperature, and each other, design tradeoffs can not be easily estimated with a simple analytical expression. The TTT diagram enables visualization of gettering process optimization. The simulator and its use to generate TTT diagrams respresent a transformation of the understanding of gettering in device processing from isolated trends and accumulated intuition to an integrated picture that can be drawn upon to engineer TM gettering into device process design.

Thesis Supervisor: Lionel C. Kimerling
Title: Thomas Lord Professor of Materials Science and Engineering

Acknowledgments

I want to express my sincere appreciation for the guidance, enthusiasm, and insights bestowed upon me by my thesis advisor, Prof. Lionel C. Kimerling. His lab and research program afforded me an rare opportunity to pursue research on photovoltaics and he has introduced me to the fascinating world of defects in silicon, a field to which he has made many noted and important contributions. I also want to express my sincere gratitude to the members of my thesis committee, Profs. Weunsch and Marzari, for their helpful suggestions, support and encouragement.

I deeply appreciate the attention, guidance, and lab-savviness of Dr. Jurgen Michel. I also appreciate his enthusiasm for discussing ideas and giving constructive feedback. He has done a great job of giving the simulator a user-friendly front end so that it is now accessible to PC users in the wafer-growing industry. I have enjoyed the support and discussions with many researchers in the emat group: Dr. Xiaoman Duan, Dr. AnneLena Thilderkvist, Dr. Anuradja Agarwal, Dr. Michal Lipson, Dr. Kazumi Wada, Dr. Anat Eshed, Dr. Mitra Marenzi, Dr. Laura Givone and Dr. James Foresi, Dr. Kevin Chen, Dr. Thomas Chen, Dr. Desmond Lim, Dr. Kevin Lee and Dr. Andy Luan, and Julia Chan. I have benefited greatly from the collaboration of Dr. Gerd Norga, Dr. Song Zhao, Dr. Sang Ahn, Lynn Chalfoun, Marlene Platero, Andre Kelley, Ashley Salomon, and Dr. Bertram Langhanki. I am thankful to Sajan Saini for Pl help and along with my other officemates, Shoji Akiyama, Donghwan Ahn, and Preston Li, for providing a supportive and enjoyable environment. I appreciate the DLTS help of and enjoyable talks with Jessica Sandland. I enjoyed working with great people at Siemens Solar Industries: Grace Xavier, John Coleman, Alex Mikonowicz, and Marie Drape along with many others.

I have benefited from the opportunity to work with Prof. Sadoway in the freshman solid state chemistry course. His enthusiasm for teaching and learning is infectious. I have been grateful for the chance to learn from Profs. Rose, Allen, Carter, Ross and Kolodziejski. I appreicatiate the support of Angelita Mireles and Kathleen Farrell.

At points in my life when people of a similar mind have not been available, I

have turned to the support of authors, living or dead. Stephen J. Gould took on the tedious task of debunking recent attempts to "scientifically" rank the intelligence of groups of people. Howard Zinn taught me the line "If you don't know anything about history, it is as if you were born yesterday. You will believe *anything*." David Noble was there to fill in that history, particularly in regards to how Western Science has evolved as a protected male-enclave from its roots in the European monastic tradition. One of my favorite author-friends is Virginia Woolf who simply ridicules suppositions of female-inferiority in such a damning, intelligent, and witty manner, that she makes it impossible for them to have any hold over me. No one puts things into clearer perspective than Dr. Vandana Shiva.

I have been fortunate to find so many wonderful people at and around MIT who *have* been of a similar mind. Working with the MIT Social Justice Cooperative has been an incredibly positive and invigorating experience for me, and has enabled me to meet and work with incredible people. The beauty and love of those who are willing to put fears aside as they struggle for justice is deeply moving. My love, prayers and thanks to everyone in the movement against the dominence of global capital, militarism, racism, sexism, classism, nationalism and envirnmental degradation. My hope rests in the success of the movement for increased democratic participation and control, for the implementation of the Universal Declaration of Human Rights which recognizes the sanctity of all human life,and for long-term focused stewardship of our precious and very threatened eco-system. My respect and thanks go out to Profs. Noam Chomsky, Jonathan King and Robert Silbey, Tina Pihl for important thesis work and her friendship, Zhelerentice Scott for her inspiring approach to life, Julia Steinberger for her perpetual effort and compassion, Brice Smith for his tireless efforts to advance women's rights, his equally tireless friendship, and his paper-mache skills, Saurabh Asthana for caring enough to learn about feminism and trusting enough to teach me about racism, Michael Borucke for his great Tech articles and his support, Aram Harrow for making me laugh and email debating skills, Dave Strozzi for trying to make me laugh and getting so many things done, Eric Hetland for his persevering and patient manner, Gil Obler for knowing about the gender-cleansing of science, Sanjay Basu for his energy, Martin Hunter for his initiative and his drumming, Stephanie Wang for her youthful realism, Gabrielle Magro for her fearless independence and laugh, Jan Outcalt for her courage and her wisdom, Eser Keskiner for his warmth, Mehdi Yahyanejad for his courage, Michelle Pvonelli for her enthusiasm and photography skills, Chuck U, Linda P, Mark Weaver and DeWayne Dickerson for their wisdom and radio skills, Ken Ostrander for never being phased, Scott Cooper for his media skills and his patience with anarchists, and Felix AuYeung for his mature idealism and inspirational spirit.

I have been fortunate to find many other friends here at MIT. Nicole Zacharia, Brandon Wood and Manish Deopura are wonderful to work with, Jessica Young has been an inspiration, James Sarvis and Stacy McGeever have been great coaches and friends, and Tessa Warren has been a great support. Thanks to Susan Dacy for her constant friendship and to Olivera, Pei, Kari, Alicia, Lindee, Eli, Kathy, Chrissy, Nancy and all the great women of the MIT ultimate frisbee powerhouse. Thanks to Elaine Tirrell, Elisabeth Shaw, Hilary Sheldon, Blanche Staton, Ayida Mthembu, Dr. Judith Klein and Dr. Sridhar Seetharaman for support and encouragement.

I appreciate many friends from before coming to MIT. Working with Dr. Shouleh Nikzad was a wonderful experience. She more than any other has been my inspiration and role-model. I appreciate the friendship and support of Dr. Douglas Bell, Dr. Nirupama Sharma, Dr. Ludger Eckey, Jeff Hagen, Coach Jim and Lupe O'Brien, Paul Socolow, Amy Meekins, and Dr. Jennifer Disney.

Thank you to my parents for giving me life, love, and the freedom to become my own person. Thank you for teaching me about honor, justice and the inherent value of all of God's creations. I deeply appreciate the love and support of my sister Jennifer Mazarr and her wonderful family. I treasure the depth of searching and love of my oldest brother Aaron. I appreciate the support of my brother Nathan and his wife Lorelei. If my younger brother Adam is a glimpse of the future, there is much reason for me to hope. I am grateful for the love, support and encouragement, of my schoonmoeder, Paula and my schoonvader, Juris. I deeply treasure my best friend, Anton.

Contents

List of Figures

Chapter 1

Introduction

In a world where 815 million people go hungry [1], the opportunity to study the laws of nature is a tremendous luxury. As scientists, we are trained to follow the *Scientific Method* of postulating a *hypothesis,* testing these suspicions, and determining whether they serve to generate a framework of understanding, or a *theory* . In Francis Bacon's ideal, we must pursue this project in a blindly judicious manner that leaves us unemotionally committed to a particular outcome and thereby as open as possible to whatever truths Nature chooses to reveal to us. Furthermore, in the Western tradition of science in which Bacon is a figure of mythic import, it is taken as axiomatic that this pursuit of knowledge is beneficial to the positive development of human society. Many times the results of these theories themselves have impacted the way in which we understand this collective human project called *science.* In quantum mechanics, for example, we learn that our observation of events fundamentally changes the course of events and we are no longer able to conceptualize ourself as the observer severed off from Nature, but as an inextricable participant residing *within* and dependent *upon* the natural world. We scientists, whether we accept it or not, have been slowly transformed from rapacious coaxers and dominators of Nature to her vulnerable, self-conscious subjects. In this position of humility, we find Thomas Kuhn's conception of science has overtaken Bacon's and we can begin to see that our reductive scientific understanding of Nature is not equivalent to *knowing* nature, but rather that science is a socially constructed language that describes the behavior of ourselves and environs in ways that are communicable from one human being to another. As we remove the layers of myth and abstraction, we come to see that we are not blind, detached, objective observers of our universe, but actors and participants within it with various culturally generated allegiances and biases. Like all collective human projects, science is prone to subjectivity. From the very framing of questions, to the prioritizing of topics, to the amount of financial resources society as a whole is willing to make available for a particular field of study, science is shaped by personal and collective bias. As good scientists, it makes sense to turn our method on both our own personal bias and the axiom of whether our work is able to live up to our own personal definition of service to humanity. In addition, we must turn our method upon the bias of our society as a whole in terms of promoting our particular field of interest and enabling service to the interests of humanity.

1.1 Photovoltaics in the World Energy Market

The number of variables and forces acting in any physical system is immense. In order to develop a model of the system, all but the dominant forces are neglected. The study of world events is no different. The number of variables, forces, and interactions between all of these creates a complexity in human affairs that is perhaps unparalleled. Those interested in the development and deployment of low environmental impact technologies such as photovoltaics need to have a firm assessment of the dominant barriers to making this vision a reality.

The current world economy is driven by fossil fuels. Just as with the cotton driven world economy that came before, the imperial power or powers of the world seek to control the central commodity, not only for reasons of profit, but for strategic control over the economies of other empires or potential empires. As with the cotton economy, control overrode ethical considerations as Britain colonized India, smashing its highly developed textile industry, dominated Egypt's production of cotton, and various of its colonies participated in that "peculiar institution" known as chattel slavery [2]. Now we are reaching a unique point where the irrationality of ignoring ethical considerations could alter or destroy all life as we know it, yet the systems that are set up to amplify power at all costs are not easy to redirect. Alternative power generating technologies suffer from two major defects from the point of view of global domination: i.) they are decentralized and therefore, difficult to keep under the control of a small group of wealthy elites, and ii.) they have to compete in a marketplace that is heavily skewed through government interference towards the technologies that satisfy criterion i.) This unregulated obsession with power and growth in a finite planet is best modeled as a cancer where its lack of feedback mechanisms may inevitably lead it to kill the host, ending all life as we know it. In spite of the systems put in place in our society to amplify power and global dominion, it is people who ultimately carry out the steps to make it happen, granted via a complicated web of actions and interactions. If enough people figure out how to turn their collective love of humanity, the planet, and all life on earth, into collective action that redirects our collective course, then our destruction can be avoided, or at least forestalled. If these irational driving forces can not be brought into control in time, then hopefully we have made of this existence the most we could. In hopes of the former path for humanity winning out over the latter, the more tools we have to help us slowly reduce our addiction to energy and the excessively consumptive and exclusively material focused life that comes with it, the better our chances of creating a sustainable way of coexisting with our planet and all the flora and fauna who call it home. Toward this end, I toss my efforts in the direction of improving solar cell efficiency and manufacturing by the control of transition metal contamination.

1.2 Solar Cell Structure

The vast majority of terrestrial based photo-voltaics are made on silicon technology. Silicon is an attractive material system, and not only because it is readily available and environmentally benign in the solid state. The central importance of Si to the field of integrated circuits (IC) has made it one of the most thoroughly studied materials

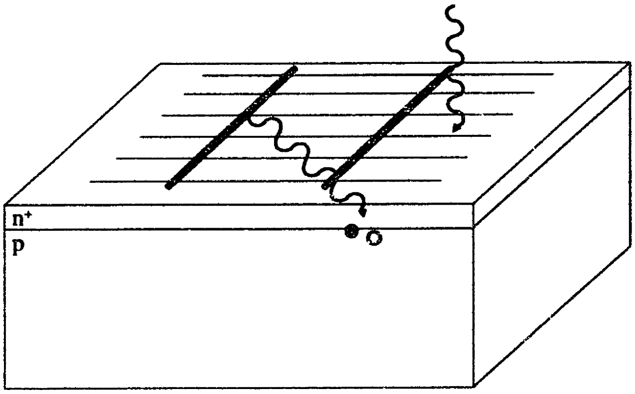

Figure 1-1: A typical solar cell device structure.

systems to date, providing Si solar cell engineers with an extensive technological data-base and serves as a way around the dearth of resources committed to solar cell research. Si has a suitable band-gap for sunlight at the earth's surface. Photons of energy exceeding the silicon energy band gap generate electron-hole (e-h) pairs that can be separated by a p-n junction and used to do electrical work in an electrical circuit. On the negative side for Si is the fact that its indirect band-gap makes it relatively inefficient at absorbing incident photons, requiring a significantly thicker device than that required for a direct-gap semiconductor system.

1.2.1 p-n junction

While there are various strategies in design, the majority of cells are based on a single p-n junction formed on a multi- or single-crystalline silicon substrate. The p-n junction in equilibrium generates a depletion region on either side of the junction due to the diffusion of majority carriers across the junction. The depletion region has an electric field across it which serves to prevent further outdiffusion of the majority carriers from their respective sides of the junction. The potential across the device

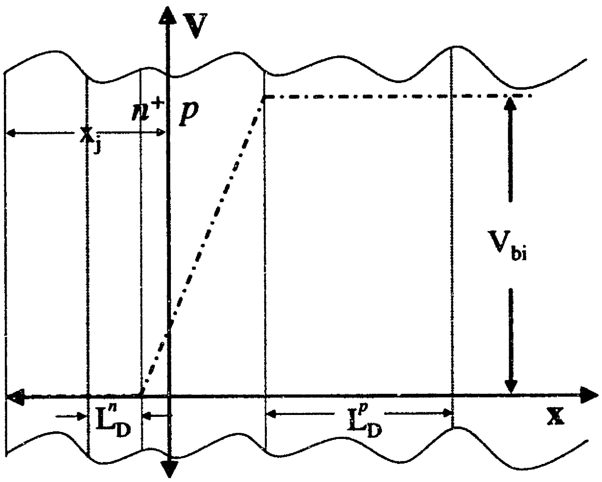

Figure 1-2: The p-n junction in a solar cell.

is depicted in figure 1-2. When e-h pairs are generated by absorbed photons, the minority carriers diffuse until they either reach the field region of the junction depletion region and do electrical work or until they recombine with a majority carrier and do no work.

The minority carrier lifetime, τ, is a measure of the characteristic time until recombination with a majority carrier. The minority carrier diffusion length, L, is given by:

$$L = \sqrt{D\tau} \tag{1.1}$$

where D is the diffusivity of the minority carrier. The effective active area of the solar cell is then given by the the junction depletion region and the minority carrier diffusion lengths on either side of the junction. The most typical structure is an n-type region diffused into a p-type substrate in order to take advantage of the higher mobility and thereby increased D of electrons over holes as minority carriers. The remaining determiner for internal quantum efficiency is contained in τ making it the relevant materials parameter to optimize for solar cell efficiency.

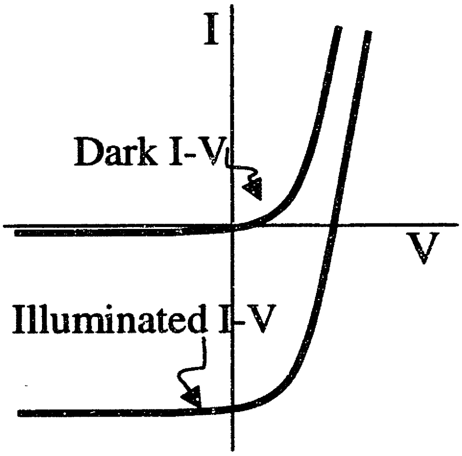

Figure 1-3: Solar cell I-V characteristics.

Figure 1-3 shows the current (I) voltage (V) characteristics of a solar cell. The device operation is in the third quadrant, and ideally, the cell is loaded to operate at the knee of the curve.

The net rate of recombination, τ_{net} is a sum of the recombination rates that occur in parallel: recombination due to Auger processes, τ_{auger}, recombination rate due to each impurity or defect, i, which follow Shockley-Read-Hall statistics, τ^{i}_{SRH} and recombination due to diffusion of minority carriers to defect states associated with the wafer surfaces, $\tau_{surface}$. Accordingly,

$$\frac{1}{\tau_{net}} = \frac{1}{\tau_{auger}} + \sum_{i} \frac{1}{\tau^{i}_{SRH}} + \frac{1}{\tau_{surface}} \tag{1.2}$$

As equation 1.2 demonstrates, the recombination mechanisms with the shortest lifetime dominate while those mechanisms with much longer lifetime can be neglected. Auger processes involve e-h pair recombination where the energy released in the process is conserved by excitation of an additional free carrier. This process has first order reaction kinetics for the minority carrier and second order reaction kinetics for the majority carrier. The Auger recombination mechanism, therefore, becomes significant in the presence of heavy doping or when the generated carrier concentrations exceed the equilibrium majority carrier concentration, a condition called high level injection. For solar cells under what is termed *one sun illumination* , or under sunlight that has not been concentrated with external optics, the high level injection regime is not entered. For most cell designs, the doping levels are not high enough to make Auger recombination a significant recombination mechanism. Surface recombination is highly dependent on the cell geometry and surface treatments. Most of the Si cell industry currently uses a process that generates a back surface field which repels minority carriers from the back surface, significantly reducing the impact of the surface recombination mechanism. We turn our attention to what is often the dominant recombination mechanism in Si solar cells, the various contaminants with minority carrier τ^i_{SRH}.

The Shockley-Read-Hall model quantifies the impact of deep level traps presented by impurities or crystallographic defects. Defects that present states for carriers in the forbidden energy gap of the semiconductor serve as spatially localized stepping stones facilitating e-h pair recombination. The efficiency with which a particular trap serves to capture carriers of each type is partly dependent on the detailed nature of the defect and partly dependent on the position of the trap within the gap. Traps that are located near the center of the energy gap simultaneously minimize the energy emitted by capture of each type of carrier needed for pair recombination. These deep states have the most deleterious effects on τ_{net}. The dependence of τ^i_{SRH} is given by the following relation:

$$\tau^i_{SRH} = \frac{1}{\sigma^i N^i_T v_{th}} \qquad (1.3)$$

where σ^i is the trap carrier capture cross section, a measure of how good the particular trap associated with species i is at capturing minority carriers, N^i_T is the concentration of species i, and v_{th} is the thermal velocity of the minority carrier, or the average magnitude of the velocity of the carrier between scattering events. From equation 1.3, we see that the minority carrier lifetime of our material is inversely proportional to the concentration of traps.

1.3 Impact of Transition Metal Impurities

Many transition metal (TM) impurities are known to introduce deep states in the energy gap reducing τ_{net} and thereby solar cell efficiency. There are many sources of TM in a solar cell manufacturing facility, including residual metal contamination in the more inexpensive grades of Si starting material. For these reasons, there is considerable interest in controlling TM contaminants in a manner that minimizes their negative impact on cell performance. To make progress towards this goal, we need to develop our understanding of the most pervasive contaminants, the degree to which these contaminants affect τ, and the relevant thermodynamics and kinetics of these impurities in the Si system. Clearly, we would like to use this understanding to eliminate the mechanisms of TM introduction wherever reasonably possible. However, the harsh cost-constraints on the solar cell industry will often necessitate tolerating low cost Si as the starting material, extended wet-chemical bath lifetimes, and cost cutting against other clean environment equipment making some degree of TM tolerance necessary.

1.4 Defect Control For High Yield Production

Many TM impurities in Si reside on interstitial sites and have substantial diffusion coefficients, as is typical with interstitial species. Diffusion coefficients as a function of temperature are presented in figure 1-4 [3].

Transition metals with substantial solubility limits in Si can significantly reduce τ. Solubility limits for some transition metals are presented in figure 1-5 recorded in a review of TM in Si processing by Graff [3].

The ability to move TM contaminants out of regions where they present a deleterious impact on device operation into regions where their presence is benign is called *gettering*. By understanding the thermodynamic driving forces and kinetic responses

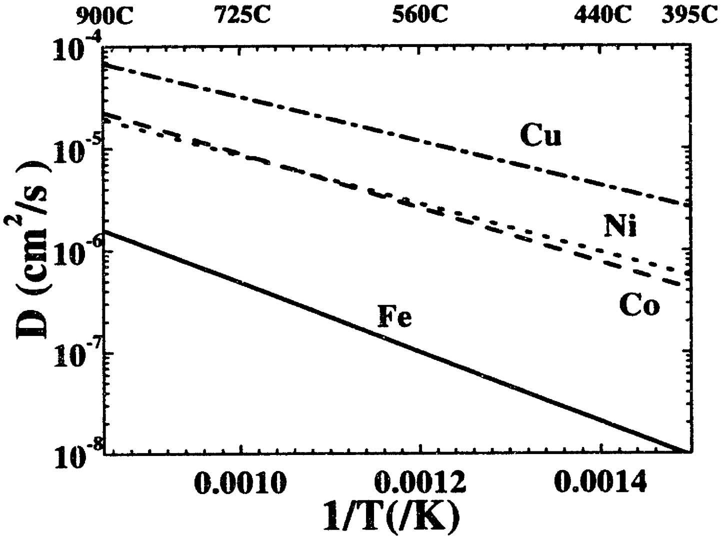

Figure 1-4: Coefficient of diffusion for common transition metal impurities.

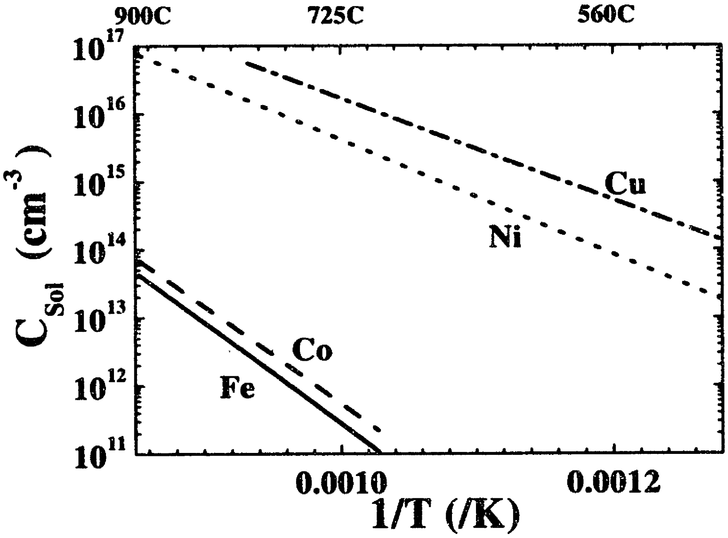

Figure 1-5: The solid solubility limit for Fe, Cu, Ni and Co in Si [4].

of TM in various regions of the cell structure, we can model the impact of various time-temperature profiles associated with typical processing sequences on TM redistribution and gettering.

In the case of IC fabrication, the device is contained in the near surface region. Successful gettering for the IC application is a matter of moving contaminants away from the surface and into the bulk. In the solar cell application, the active region of the device penetrates a significant distance into the bulk. Optimal gettering requires removal of TM from the bulk. Aggregated impurities can result in better or worse τ depending on the electrical properties of the aggregate. Metal silicide precipitates will be less numerous than dispersed metal contaminants, but in some cases, the defects produced by the silicide can over-compensate this reduction in N_T with an exceptionally high σ^i.

In this thesis, we have investigated three aspects of the TM gettering: i) the adequacy of high temperature Si data, ii) simulation of processing and wafer parameters on gettering with an effective means to display the results, and iii) comparison of our gettering understanding to experiment.

1.4.1 Si Data at Processing Temperatures

In order to enable predictive simulation of gettering processes in the *processing* temperature regime (700-1400K), we need to develop a better understanding of intrinsic Si at these temperatures. Much of our understanding about Si is based on data from very low to room temperatures, the *measurement* temperature regime (4-400K), which has a good degree of overlap with typical operation temperatures of semiconductor devices, or the *operation* temperature regime (200-400K) enabling reasonably accurate device simulation and design. Since we are interested in extrapolating our Si data to much higher temperatures for the purpose of quantitative modeling and simulation of thermodynamic and kinetic processes at the high temperatures used during device fabrication, we need to carefully consider the adequacy and accuracy of these extrapolations.

1.4.2 Simulation

We use what is known about TM defect thermodynamic driving forces and kinetic responses to make possible predictive simulation of gettering during solar cell fabrication. We have developed a simulator to explore the impact of various device and process parameters on gettering effectiveness. The relevant heat treatments are ramps up in temperature, isothermal annealing, and cools from high temperature down to room temperature. We explore a range of surface conditions, density and size of heterogeneous nucleation sites in the bulk, and the degree of contamination in order to create a framework in which to examine these mechanisms acting in concert and to enable process optimization for gettering.

1.4.3 Process Design TTT diagram

Using the simulator, we have generated time-temperature-transformation diagrams, or TTT diagrams, to enable presentation of the effect of the iso-thermal heat treatment for a given set of wafer parameters over a range of times and temperatures. The equilibration curve gives the time to reach the point in gettering where no more driving forces remain. Iso-concentration curves allow demonstration of when, if ever, particular specifications for residual contaminants levels have been achieved at each temperature.

The TTT diagram provides an overview of the gettering potential of the particular wafer design. An optimal cooling curve can be determined from the diagram for a particular wafer design based on the TM specification. Wafer parameters can be compared via their respective TTT diagrams and the various likely contaminenets can be examined collectively to ensure a compreshensie gettering strategy.

1.4.4 Experimental Results

Fe gettering experiments were carried out under conditions of supersaturation with various surface treatments. We use our model of Al segregation and internal gettering to simulate these gettering treatments and demonstrate their predictive capability for gettering at 810°C based on data fit at 755°C. The discrepency between simulation and gettering data from treatment at 695°C reveal that silicide growth on the inside of the wafer is retarded on samples with Al contacts relative to those with $FeSi_2$ contacts. We propose a point defect mediated mechanism interaction analogous to the case of SiO_2 growth in Si to explain the gradual shift from Fe diffusion limited kinetics to a slower mechansim as the treatment proceeds.

Cu gettering studies were carried out on p/p^+ epitaxial wafers and polished FZ wafers and analyzed with photoluminescence (Pl) spectroscopy and selective etching. Pl revealed that impurity segregation from the lightly doped region to the heavily doped region has occurred. Etching revealed significant density of defects below the epitaxial layer, giving additional confirmation of the segregation effect.

1.5 Thesis Structure

In Chapter 2, I will present an overview of what is known about the solubilities and diffusivities of TM's in the silicon solid solution, how doping affects these properties, and the state-of-the-art in understanding of the underlying intrinsic silicon properties in the processing temperature regime.

In Chapter 3, I discuss solubility driven redistribution from a lightly doped region to a heavily doped region and from silicon to a molten Al phase. The segregation coefficient for redistribution is derived and calculated results for both cases are presented.

Chapter 4 provides an overview of heterogeneous and homogeneous nucleation and growth of the silicide phase of various transition metals in silicon.

Chapter 5 contains the process simulator, results, and the generated TTT diagrams that can serve as a process design diagram.

In Chapter 6, I present experimental results of Fe and Cu gettering studies carried out on p-type Si. For the case of Fe gettering, we demonstrate that simulation at high temperatures is predictive, but that at lower temperatures, consideration of point defect equilibria is needed for adequate simulation. For the case of Cu, we demonstrate the gettering capacity of heavily p-doped substrates by the eliminating Cu PL signal from the lightly doped epitaxial layer and by the presence of haze in the substrate just below the epitaxial layer.

Chapter 7 contains the summary of achievements and recommendations for future work.

Chapter 2

Transition Metal Defects in Silicon

Transition metal (TM) contaminants have deleterious effects on silicon device performance. To understand how TM contaminants are introduced into the Si crystal during growth or casting and subsequent device processing, we need to develop as complete a picture as possible of the *thermodynamic driving forces* for contaminant incorporation and redistribution, the *kinetic barriers* that limit the response to those driving forces, and the manner in which each of these are affected by processing time and temperature and by device and substrate design parameters.

2.1 The Solid Solubility Limit

2.1.1 Intrinsic Si

We begin our study of the thermodynamics of TM contaminants in Si with the solid solubility of the TM in intrinsic Si as a function of temperature. Solid solubility is defined as the maximum equilibrium concentration of solute in the solid solution as dictated by the Gibbs free energy curves as a function of composition. For a particular temperature and pressure, we schematically represent the Gibbs free energy curves in figure 2-1. The maximum mole fraction of solute in the solid phase α, x_{sl}, will be found when a common tangent is constructed between the α phase and the β phase as depicted in the diagram. The common tangent construction arises because

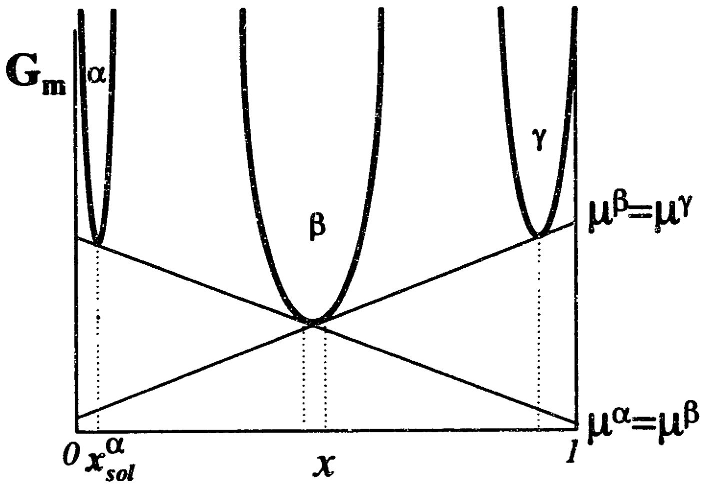

Figure 2-1: The solid solubility limit for a contaminant in the α phase is determined by the common tangent construction.

the system can minimize its Gibbs free energy better by splitting into two phases of appropriate phase fraction, rather than moving up in free energy on one or the other phase Gibbs free energy curve. When the system is in equilibrium, it will minimize its Gibbs Free energy by lying on the hull created by making an envelope of the Gibbs free energy curves and the common tangents.

As with most real world systems, we are concerned with equilibrium properties at fixed pressure of 1 atm. We are interested in the temperature dependence of the solid solubility limit, as temperature is one of our fundamental process variables during device fabrication. For the case where the solid solubility is given by the common tangent construction between the α phase and a phase of fixed composition, such as an intermetallic compound, the composition has an Arhenius dependence.

We can demonstrate this with a particular example. For the case of Fe solid solubility in Si, which we refer to as the α phase, we mean the concentration of the Fe in solid solution, while the solid is in contact with the $FeSi_2$ phase. Equivalent to the common tangent construction is the requirement that the chemical potentials of Fe and Si are equal in both phases.

$$\mu_{Fe}^{\alpha} = \mu_{Fe}^{FeSi_2} \tag{2.1}$$

$$\mu_{Si}^{\alpha} = \mu_{Si}^{FeSi_2} \tag{2.2}$$

For highly dilute solutions, we can approximate the Gibbs free energy, G(x), for the α phase with an ideal solution model.

$$G^{\alpha}(x) = x\mu_{Fe}^{o} + (1-x)\mu_{Si}^{o} + k_BT\left((1-x)ln(1-x) + xlnx\right) \tag{2.3}$$

where x is the mole fraction of Fe in the binary system and μ_{Fe}^{o} and μ_{Si}^{o} are the chemical potentials of the pure Fe and Si states respectively in the α phase. The chemical potentials of Fe and Si can be written as:

$$\mu_{Fe}(x) = G^{\alpha}(x) + (1-x)\frac{\partial G^{\alpha}}{\partial x} = \mu_{Fe}^{o} + k_BTlnx \tag{2.4}$$

$$\mu_{Si}(x) = G^{\alpha}(x) - x\frac{\partial G^{\alpha}}{\partial x} = \mu_{Si}^{o} + k_BTln(1-x) \tag{2.5}$$

The Gibbs free energy of the intermetallic compound if we neglect off-stoichiometry, is given by the common tangent rule is given as follows:

$$G^{FeSi_2} = \mu_{Fe} + 2\mu_{Si} \tag{2.6}$$

Solving for the x_{sl} satisfying the common tangent construction gives:

$$x_{sl} = exp\left(\frac{G^{FeSi_2} - \mu_{Fe}^{o} - 2\mu_{Si}^{o}}{k_BT}\right) \tag{2.7}$$

This relation can be converted to concentration units and the Arrenhius form as follows:

$$C_{sol}(cm^{-3}) = 5x10^{22}exp(\frac{\Delta S}{k_B})exp\left(\frac{-\Delta H}{k_BT}\right)(cm^{-3}) \tag{2.8}$$

[3] Where ΔS and ΔH are the entropy and enthalpy of solution. Above the eutectic temperature, this model is not valid as the liquid phase has variable composition, but it is known that the solubility limits for most transition metals are retrograde and have their maximum at temperatures above T_{eut}. Figure 1-5 experimental data for solid solubilities of several transition metals as a function of temperature [4]. The figure demonstrates that while many of these impurities have appreciable solubilities at the high temperatures of the device processing regime, the large ΔH, or enthalpy of solution, means the solubility limit falls precipitously with temperature.

2.1.2 The Effects of Doping

The presence of a third element then requires consideration of ternary Gibbs free energy curves and the ternary phase diagram. In order to determine the affect doping will have on the TM solubility limit, we will need to consider the ternary phase diagram of Si, the TM and the dopant atom. There are two ways in which dopants can affect the solubility limit of a TM, i.) by forming complexes with the TM and ii.) by affecting the equilibrium electron and hole concentrations to affect ionization reactions of the TM in solution. This latter process, as pointed out by Reiss [5], can be thought of as the solid state analog to the common ion effect in solution chemistry where electrons or holes play the role of the common ion. Both types of processes can be represented as point defect reactions which are mediated in various ways by the semiconductor solid solution that serves as the host.

For the case of Fe in p-type Si, the relevant reactions are as follows:

$$Fe_{ext} \rightleftharpoons Fe_i^o \tag{2.9}$$

$$Fe_i^o \rightleftharpoons Fe_i^+ + e \tag{2.10}$$

$$A_s \rightleftharpoons A_s^- + h \tag{2.11}$$

$$null \rightleftharpoons e + h \tag{2.12}$$

$$Fe_i^+ + A_s^- \rightleftharpoons Fe_i^+ A_s^- \tag{2.13}$$

Where Fe_{ext} is Fe coming from an external phase, such as $\mathrm{FeSi_2}$, Fe_i^o and Fe_i^+ are neutral and ionized interstitial Fe in Si, e is an electron, h a hole, and A_s^o and A_s^- are the neutral and ionized substitutional acceptor respectively. The charge neutrality condition

$$[Fe_i^+] + p = [A_s^-] + n \tag{2.14}$$

must also be satisfied.

Many of these reactions contain charge carriers and subsequently will have an equilibrium constant that is dependent on the electro-chemical potential of e or h, or the fermi level (E_F).

In order to understand how to include these species correctly in our models, we should first revisit the essential features of semiconductor band theory to appropriately model their behavior in these reactions.

Si: Setting the Stage

The discrete nature of electronic levels in atomic species can be solved quantitatively for the case of a one electron system using the Schrödinger Equation with a central potential. For a simple bond occupied by one electron, straightforward quantum mechanics can again be applied to determine the equilibrium distance for the bond and whether it will be stable. Bringing additional electrons into the picture complicates the ability to solve the equation due to the delocalized nature of the interaction between electrons in the system, namely the effects of exchange and correlation. Nevertheless, qualitative undertstanding of molecular bonding and anti-bonding orbitals of the molecular oribtal theory are easily acheived. By extention of the molecular orbital theory, at least at a very qualitative level, we can see how the generation of a solid with on the order of 10^{23} atoms will generate bonding and anti-bonding levels that are so close together in energy that they are essentially smeared into bands of allowed electronic states. In the case of a semiconductor or an insulator, not only are there gaps or fobidden energies between bands, but these states fill with the system's electrons via the Pauli Exclusion principle exactly to the top of one of these bands at zero Kelvin. In the case of a semiconductor, the energy required to cross the band gap, E_G, is low enough for some degree of thermal activation to occur at typical device operation temperature, roughly set at $E_G < 3\text{eV}$. In Si, the valence and conduction band are formed from sp^3 hybridized bonding and anti-bonding molecular orbital states, with the N Si atoms completely filling the valence band with their 4N valence electrons, two to each of the 2N bonding states.

Each electronic state in a solid has both an energy and a wave vector, $\vec{k}$, or crystal momentum associated with it. For a semiconductor such as silicon, the maximum filled state in energy is called the valence band edge, E_v, and the minimum energy state unfilled at 0K is the conduction band edge, E_c, which is separated from the valence band edge by $E_G(0K)$. Each state can then be occupied by two electrons, one of each spin, unless the spin state interacts with the energy state to break the degeneracy. This interaction of spin with the other quantum numbers of the state is called spin-orbit coupling and it does play a noticeable role in the valence band of Si.

While we are primarily interested in the nature and temperature dependence of the bands to understand the impact they have on carrier statistics, the curvature of these can be related to the dynamics of quasiparticles, *electrons* and *holes*, in the solid as formulated by the *effective mass theorem*. An electron in the conduction band has access to many states and can be easily accelerated in any direction. For this reason, only electrons in the conduction band are referred to as conduction electrons. The absence of an electron in the valence band allows electrons to respond to outside potentials and conduction of what is called a hole can take place. Both of these carrier types can be thought of as quasiparticles that are modeled as free carriers responding to a perturbing potential, with the affect of the presence of the crystal on the carrier being captured in an effective mass, m^*, that replaces the free electron mass, m_o.

The curvature of the band extrema determines the effective mass tensor. Close to the extremum, it can be approximated by a Taylor expansion.

$$E(\vec{k}) = E(\vec{k_o}) + \frac{1}{2}\sum_{i,j}\frac{\partial^2 E}{\partial k_i \partial k_j}(k_i - k_{io})(k_j - k_{jo}) \tag{2.15}$$

where i and j are x, y, z and k_i, k_j represent the respective components of the wave vector $\vec{k}$. The coefficients from the Taylor expansion generate a tensor of rank 2 which can be diagonalized with appropriate choice of k-space axes and the effective mass for each direction can be defined:

$$m_i^* = \hbar^2 \left(\frac{\partial^2 E}{\partial k_i^2}\right)^{-1} \tag{2.16}$$

For the case of the conduction band minimum, there are six equivalent cigar shaped ellipsoidal pockets which can be characterized by a transverse effective mass, m_t^* in two dimensions and a lateral effective mass, m_l^* in the remaining dimension. Therefore, while the conduction band is not isotropic, and its anisotropy can be represented explicitly in the Taylor expansion. The energy of the conduction band near the minimum can be fairly well approximated as for the example of expanding around the minimum at $\vec{k} = (k_x^o, 0, 0)$:

$$E_c(\vec{k}) = E_c(\vec{k_o}) + \frac{\hbar^2(k_x - k_x^o)}{2m_l^*} + \frac{\hbar^2 k_y + \hbar^2 k_z}{2m_t^*} \tag{2.17}$$

The story for the valence band is more complex. All semiconductors have their valence band maximum at the highest symmetry point, the Γ point, which occurs at the origin of k-space and designates the center of the Brillouin Zone.

While calculating the electronic bands in wavevector, or $\vec{k}$, space is a complicated taΔG^*sk, low temperature measurements give good detail about the geography of $E_n(\vec{k})$.

Point Defects: Including the Actors

Each of these reactions can be thought of as having an equilibrium constant, however in the processing temperature regime or in the presence of heavy doping when the Boltzmann approximation is no longer accurate, the simple mass balance model for carriers in Si breaks down, and the equilibrium "constant" becomes carrier concentration dependent. This is analogous to saying that the carriers in the semiconductor no longer follow ideal Henrian behavior. Next, we will review the derivation of the Equilibrium Constant from thermodynamics.

A reaction will proceed from reactants to products until the point where the Gibbs free energy difference between the two sides is eliminated. The Gibbs Free Energy difference, ΔG_{rxn}, for the reaction is given by the sum of the product of the change in number of moles of species i, ν_i with the chemical potential of that species, μ_i:

$$\Delta G_{rxn} = \sum_{i=1}^{n} \nu_i \mu_i \tag{2.18}$$

If the species behave ideally then the activity coefficient for each component is constant in changes of mole fraction and μ_i can be written as:

$$\mu_i(x_i, T) = \mu_i^o(T) + k_B T ln x_i \tag{2.19}$$

For electrons and holes in the Boltzmann approximation, we can write the chemical potential from the relation for what is called the Fermi Level, E_f or sometimes the electrochemical potential as follows:

$$E_f = E_i + k_B T ln \frac{n}{n_i} \tag{2.20}$$

When Boltmann statistics no longer reasonably approximate the behavior of free carriers, we use Fermi-Dirac (F-D) statistics. By extending the concept of e and h as chemical entities in the solid, when Boltzman statistics fail, the solution is no longer ideal or dilute in that carrier. F-D statistics are required for carrier concentrations under conditions of heavy doping, but as temperature increases into the processing temperature regime, so does the smearing of the step region of the F-D distribution function, causing E_F to be within 3 k_BT of the band edge even under condions of modest doping.

F-D statistics are typically required for calculating the ionization statistics for deep level states, such as the defect level associated with Fe_i, as these levels are often within 3 k_BT of E_F.

Modeling transition metal doping enhancement based on TM ionization reactions has been explored and experimentally verified in Li [5], Cu [7], and Mn, Co, Fe [8], and Fe [9, 10, 11, 12].

2.2 State of the Art for Si Data

A quantitative understanding of transition metal equilibria and kinetics at high temperature is needed in order to design gettering processes through accurate simulation. We continue with our focus on Fe_i, however the method is quite general and can be extended to other deep level impurities in a semiconducting host.

Researchers measuring Fe solubility enhancement due to p-type doping have found solubility enhancement to be less than they expected at temperatures above 700°C and have proposed an instability of the well known Fe_i defect level as these high temperatures are approached [8, 13]. However, as we show in our analysis, in order to infer the behavior of Fe in the processing temperature regime, we first need to complete our understanding of silicon at these temperatures. To really understand the physics of Fe at the high temperatures used in device processing, we need to begin to fill in this knowledge gap with appropriate experiments and theory.

In order to model dopant enhanced solubility of Fe in Si quantitatively, we need to understand the temperature dependence of various defect levels and Si parameters with precision. With regard to the defect Fe at very high temperatures, the Fe_i defect level, E_T, the Fermi level, E_f, and the intrinsic carrier concentration, n_i, are the controlling parameters. The Si materials parameters, E_f and n_i, are related to the effective density of states of the conduction and valence bands, N_C and N_V, respectively, and the semiconductor band gap, E_G. In the work presented here, we demonstrate that uncertainties in the Si intrinsic properties database in the processing temperature regime can account for the available dopant enhanced solubility data by assuming that E_T remains at a constant fraction of E_G.

2.2.1 DOS in the Processing Temperature Regime

Our interest in Si can be categorized into three temperature regimes: *measurement*, *device operation*, and *processing*. Most of our theoretical and experimental understanding of silicon is from very low temperatures, approximately 4-400K, in the measurement temperature regime. This temperature regime overlaps reasonably with the temperature regime of device operation, predominantly between 200K and 400K, providing accurate data for device simulation. For the case of the much higher temperatures of the processing temperature regime, approximately 700-1400K, simulations currently rely heavily on extrapolations from the measurement temperature regime. This gap in our database of Si knowledge allows for large errors in the analysis of data in the processing temperature regime. In order to predict the interaction of defect levels with E_f, we need to understand the variation of N_C, N_V, and E_G at high temperature. It is necessary to extrapolate currently available values of these parameters well beyond the range of available measurements. In doing so, we can at least gain an appreciation for how the uncertainty at processing temperatures will affect our calculations for dopant enhanced solubility of Fe in Si.

The available models for N_C and N_V disagree even in the measurement temperature regime. The routinely used $T^{3/2}$ model found in classics such as Sze's Physics of Semiconductor Devices [14] is based on a parabolic band approximation. Si, however, is known to deviate from this approximation even at low temperatures. The valence band most strongly defies this categorization due to a lack of parabolicity in energy, anisotropy in the constant energy contours, and the effect of spin-orbit coupling. At high temperatures, both bands will be more deeply probed due to the increased spreading of the Fermi-Dirac distribution function, making the parabolic approximation inadequate for both N_C and N_V. A more realistic empirical fit to data up to 500K is provided by Green [15]. Figure 2-2 shows both relations for N_C and N_V with extrapolations up to the processing temperature regime. The arrow denotes the end of the fitting regime at 500K. It is important to note that for the $T^{3/2}$ model, N_V is larger than N_C, while the opposite is true for the Green relations. This demonstrates the need to question the utility of the relations derived from the $T^{3/2}$ model even at temperatures in the device operation regime in addition to the more extreme temperatures of the processing regime. While the Green relation is a better fit to experiment, it is only valid to 500K and it is not valid when the Boltzmann approximation breaks down, such as in the case of degenerately doped material. This limitation is due to the fact that density of states effective mass is, in general, both temperature and energy dependent (see, for example [16]).

In order to generate a method for E_f determination in the processing temperature regime that is free of the parabolic assumption, we determine the 0K density of states (DOS) from first principles [6]. We use density functional theory (DFT) within the local density approximation (LDA) with the Vienna ab inito simulation package (VASP) [17, 18]. The LDA band structure-generated DOS has been shown to correlate with experiment better than the parabolic model [19]. VASP numerically solves the LDA Kohn-Sham equations using ultra-soft pseudopotentials [20, 21]. and a plane wave basis set. A cut off energy of 300eV was used. The exchange and correlation functional was that of Ceperley and Alder [22] as parameterized by Perdew and Zunger [23]. Sampling of $\vec{k}$-space was performed with the method of Monkhorst and Pack [24] using an 18x18x18 grid. Integrations of $\vec{k}$-space were performed using the linear tetrahedron method including corrections according to Blöchl et al [25]. We perform a rigid energy shift to correct for E_G which is well known to be underestimated by LDA. We then use Fermi-Dirac statistics with numerical integration and E_G(T) to determine

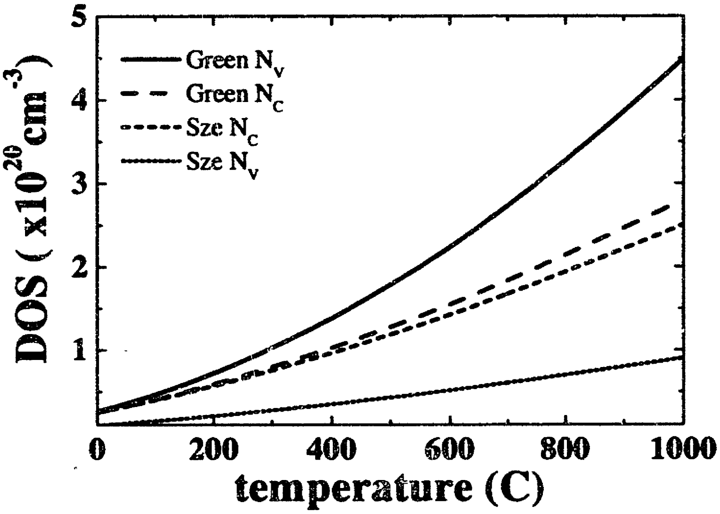

Figure 2-2: The effective densities of states, N_C and N_V for the $T^{3/2}$ and that based on the empirical fit of Green *et al* [15].

$E_f(T)$ as dictated by the charge neutrality condition. In Figure 2-3 we compare the calculated DOS with those given by a parabolic approximation to illustrate that they are very different even in the regions near the valence and conduction band edges.

The calculated DOS is subject to several approximations, even at 0K. Spin-orbit coupling is neglected, so the split-off hole band is not reproduced. In addition, LDA approximates DFT which calculates ground state energies. All of the conduction band states are excited states and thereby subject to inaccuracies, such as is evidenced by the underprediction of E_G. Qualitative features of the conduction band are expected to be reasonably accurate due to the strong influence of symmetry in determining band structure. However we cannot consider them to be quantitatively accurate.

There are additional concerns with DOS modeling at processing temperatures. Our DOS and the $T^{3/2}$ model both rely on the assumption that the band structure is not significantly altered as temperature increases. While we cannot be certain that this assumption is incorrect, there are many factors that require greater consideration before such a determination may be made. The most significant concern is that we neglect the influence of phonons on the band structure. Phonon populations

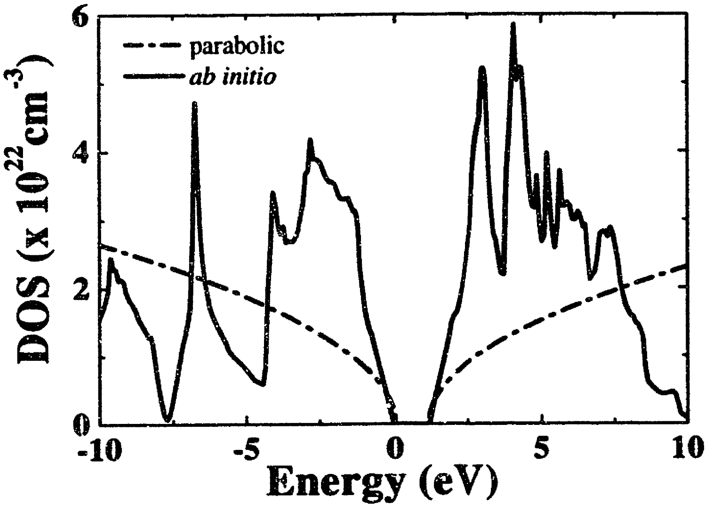

Figure 2-3: Comparison of the density of states as a function of energy obtained by *ab initio* total electron calculations to that obtained by modeling the valence and conduction bands as parabolic.

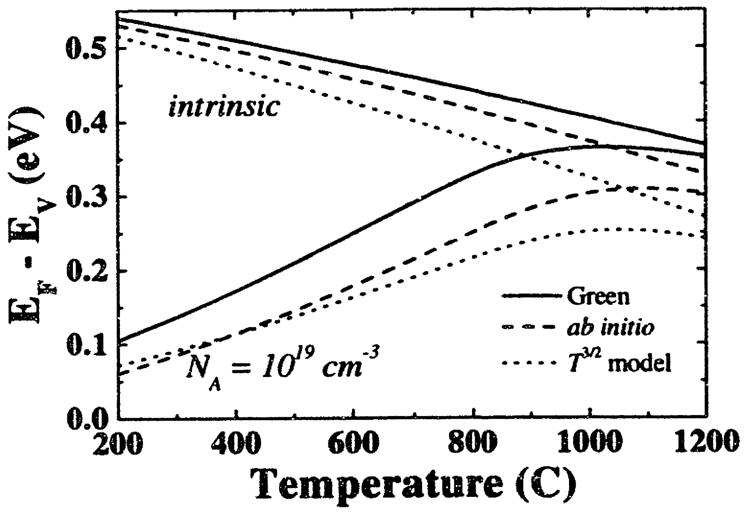

Figure 2-4: Calculated values of E_F for three different density of states approximations in the intrinsic (upper three curves) and heavily p-type doped (lower three curves) regimes. The dashed lines correspond to the *ab initio* DOS, the solid lines with the empirical treatment of N_C and N_V by Green, and and the dotted lines to the parabolic band model giving $T^{3/2}$ dependence on N_C and N_V.

will be extremely high in the processing temperature regime and neglecting their impact as we do at very low temperatures is no longer justifiable. Other factors that also need consideration are thermal expansion and the influence of the energy level occupations found at high temperature. Clearly more work needs to be done to have a comprehensive model of DOS with temperature. The method we have developed, 0K *ab initio* calculated DOS with the appropriate temperature dependent population statistics, is physically reasonable for determining E_f in the processing temperature regime, but it is by no means an ending point.

In Figure 2-4, we compare E_f for both the case of intrinsic Si and for Si with an acceptor concentration, N_A of 10^{19} cm^{-3} using the three DOS models discussed. The estimate using the *ab initio* calculated DOS falls between the curves calculated with N_C and N_V by the $T^{3/2}$ model and the extrapolation of Green's relations. In addition, it is important to note that E_f is quite sensitive to the DOS model used, varying by more than 0.1 eV at the highest temperatures shown.

Since E_f is not a measurable quantity, we look at estimates of dopant enhanced solubility generated using the different DOS models. Figure 2-5 displays calculations of Fe solubility for the case of $N_A = 1.5\text{x}10^{19}$ cm^{-3} with the various DOS models assuming E_T remains at a constant fraction of the gap. The solid line shows the intrinsic Fe solubility. The curve predicting the greatest dopant enhanced solubility was generated using again the $T^{3/2}$ model, however for this case, the Boltzmann approximation is used to determine E_f . The significant difference between this curve and that of the same DOS model with the Fermi-Dirac integrals determining E_f demonstrates the importance of using the appropriate carrier statistics. Due to the extremely high doping level, Fermi-Dirac statistics are needed.

Also in Figure 2-5 we overlay the data of McHugo, et al. The data is fit within error by the calculations using our calculated DOS method and the $T^{3/2}$ model, with no instability of E_T required. The calculation using the Green extrapolation underestimates for the data point at 1000°C. The Sze model with Boltzmann approximation overestimates the concentration at 1100°C. this is likely the source of error that led McHugo *et al.* to suggest a lowering of E_T at high temperatures.

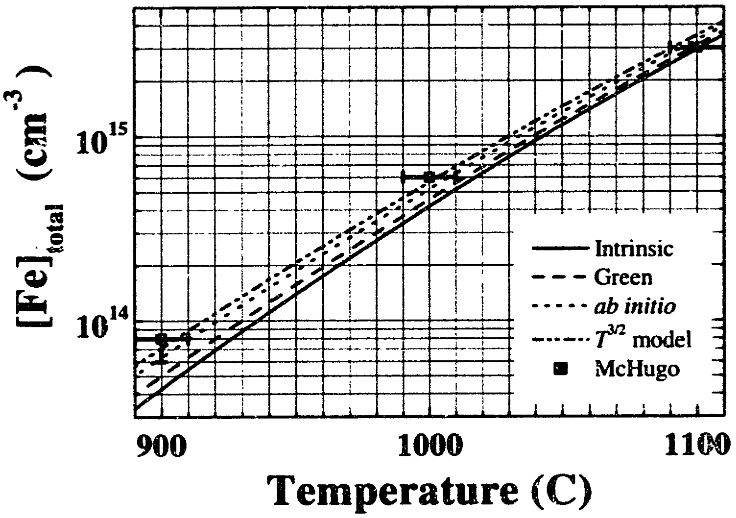

Figure 2-5: Comparison of calculated dopant enhanced solubility of Fe in Si as a function of temperature using different density of states approximation while assuming E_T remains at a fixed fraction within the band gap. N_A is 1.5x10^{19} cm^{-3}. Lines represent our caluclitions, points are Cs data measured by McHugo *et al.* [13].

2.2.2 E_G in the Processing Temperature Regime

The last parameter we require knowledge of in the processing temperature regime is E_G(T). Again, we have no reliable expression at these extreme temperatures and are left with significant uncertainty. The most commonly used expression for E_G was derived by Varshni [26]:

$$E_G(T) = E_G(0) + \frac{\alpha T^2}{T + \beta} \tag{2.21}$$

with fitting parameters valid to 750K extracted by Alex et al [27]. We have used this relation in the calculations above, but note that extrapolations of empirically based polynomials beyond their regime of validity are notoriously unreliable.

A semi-empirical expression has been developed [28, 29] and fit [30] over the 0-300K temperature range. Extrapolations to higher temperatures are consistent with extrapolations of a linear fit valid up to 415K [14]. The extrapolations of both of these

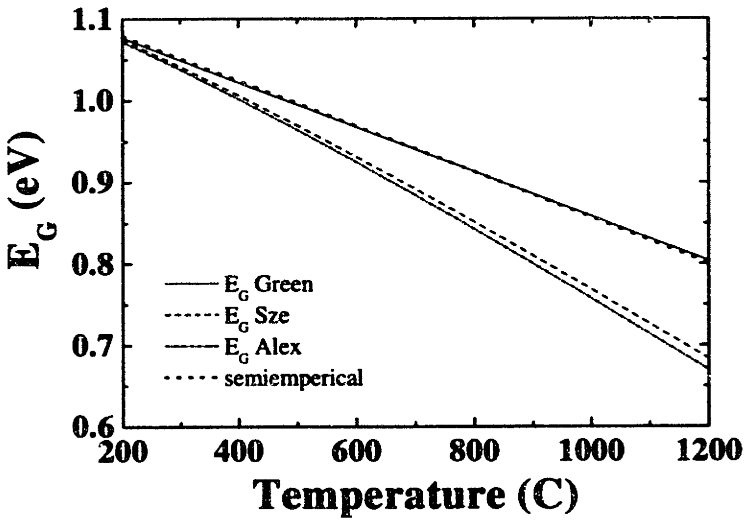

Figure 2-6: Extrapolations of various models for E_G to the processing temperature regime.

relations from 415-750K diverge significantly from the expression based on Varshni's model. Figure 2-6 shows the $E_G(T)$ for these four models. Further extrapolation of the semi-empirical model with the available parameters or the linear model of Green to higher temperatures is subject to question. Nevertheless, we calculate dopant enhanced solubility comparing the two sets of E_G(T) to observe the impact that uncertainty in E_G(T) has on our predictions. Figure 2-7 shows the solubility data with our calculations where again we assume E_T remains at a constant fraction of the gap and we use the $T^{3/2}$ model for N_C and N_V. Note that for the data point at 1100°C, the semi-empirical E_G(T) calculation is no longer within error.

While the difference in conclusions in our analysis and that of McHugo *et al.* can be explained in their likely use of the Boltzmann approximation for the carrier statistics in a regime where it was no longer valid, Gilles *et al.* did use the appropriate statistics [31]. They use the formulation of Shockley and Moll, which should produce the proper statistics on the defect level [32]. They do not publish their data above 700°C, so I can't model it, nevertheless, a likely reason for their apparent observation of E_T instability is due to failure to consider E_G narrowing due to heavy doping effects.

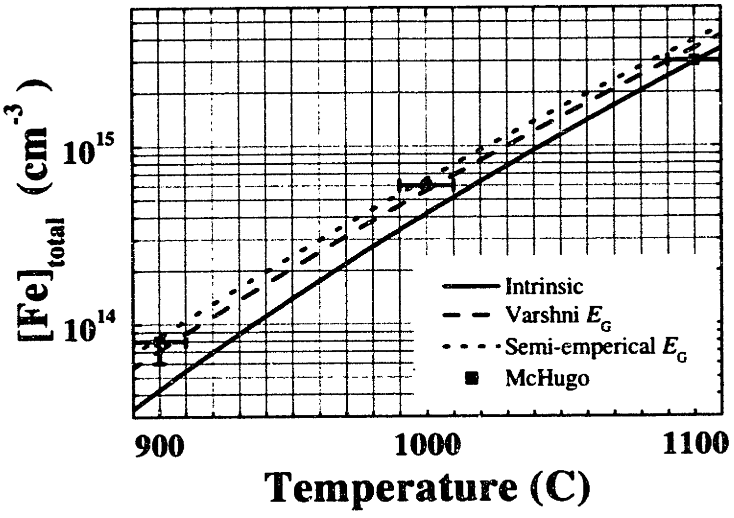

Figure 2-7: Comparison of calculated dopant enhanced solubility of Fe_i in Si for different temperature dependencies of E_G. E_T was held at a fixed fraction of the bang gap and we used the $T^{3/2}$ model

Their data was taken from samples with [B] of $8x10^{19}cm^{-3}$. The estimated ΔE_G from this level of doping is 0.11eV based on a linear model [33]. For the McHugo data, the [B] of $1.5x10^{19}cm^{-3}$ is expected to result in a ΔE_G of only .06ev. This increase in band narrowing in the data of Gilles will cause the extrinisic to intrinsic transition to begin at a lower temperature than otherwise, giving the appearence of the level moving down, when actually E_F is moving up.

2.2.3 E_T and E_B in the Processing Temperature Regime

In addition to the temperature dependence of fundamental properties of the host material, quantitative prediction of dopant enhanced solubility for a transition metal defect requires the temperature dependence of i.) the defect level in the gap and ii.) relevant parameters for reactions of the defect with other species in the host matrix. For the case of Fe in p-type Si, these parameters are E_T and E_B.

E_B is predominantly due to Coulombic force between the positively ionized Fe_i and the oppositely charged ionized dopant. A fraction of the E_B is due to covalent bonding between the species. Both of these parts, but particularly the covalent portion, could show significant temperature dependence. We neglect this dependence, but note that the likely trend is toward a decrease in E_B with increasing temperature. For the dopant enhanced solubility calculations contained in this paper, we focus on temperatures above 700°C where pairing has negligible impact on the solubility enhancement. Nevertheless, to generate a complete understanding of the dopant enhanced solubility at all temperatures, the exact temperature dependence of E_B should be determined.

Motion of E_T within the gap will clearly affect the ionization statistics and thereby the dopant enhanced solubility of Fe in p-type Si. The defect level of a species which is very foreign to its host matrix is expected to behave independently from the band edges.

We model three extreme cases of E_T behavior: i.) E_T stays at a constant fraction of E_G , ii.) E_T remains a constant distance in energy from the valence band edge, and iii.) E_T remains a constant distance in energy from the conduction band edge. Case i.) is approximately allowing the energy of E_T to remain fixed while the band edges move in temperature. Case ii.) pushes E_T towards the conduction band as E_G decreases with increasing T, and case iii.) pushes E_T toward the valence band edge as T increases. The solubility enhancement calculated for each case is shown in Figure 2-8. Defect level position does affect the results, as expected, however as noted, the case with E_T a constant fraction of E_G is within error of the experimental data.

While many have recognized that the $T^{3/2}$ model for the N_C and N_V of Si does not adequately capture some of the underlying physics of the Si bands, we note that our alternative model also has limitations, such as not capturing the spin-orbit coupling. Nevertheless, in the process temperature regime without the benefit of experimental data, we requires a new approach. To serve this end, we have developed an alternative model of Si data in the processing temperature regime based on the calculated 0k DOS for Si with temperature appropriate F-D statistics and rigid shift of the temperature appropriate value for the E_G. Using both of these methods for determining E_F, we demonstrate that doping enhanced Fe solubility measurements

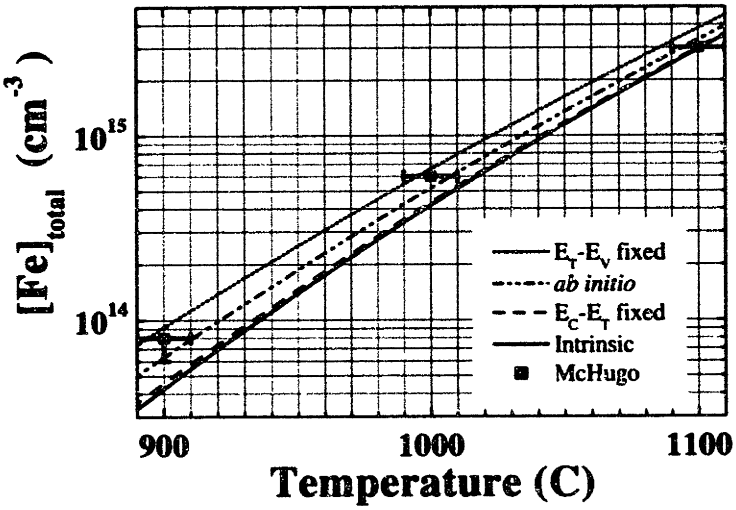

Figure 2-8: Comparison of calculated dopant enhanced solubility of Fe_i in Si for different conditions on E_T as E_G moves in temperature. The *ab initio*calculation is, as before, with E_T held at a fixed fraction of E_G, $E_T - E_V$ fixed and $E_T - E_V$ fixed refer to the solubility calculation when E_T is held at a fixed energy from the valance and conduction band respectively.

can be explained within error without necessitating a temperature instability of the E_T as researchers had previously proposed.

2.3 Transition Metal Diffusivity

2.3.1 TM in Intrinsic Si

Interstitial impurities tend to be the fastest diffusers beasue they are not dependent on the arrival of point defects to mediate a jump to a new site. The fastest TM are the focus of this work since they pose the greatest contamination risk. Diffusivity data for Fe [4], Ni [3], Cu [3], Co [34] in Si are presented in figure 1-4 in Arrenhius form.

2.3.2 The Effects of Doping

As in the point defect reaction of Fe, equation 2.13, ionized defects are known to pair with oppositely charged defects. For the case of ionized dopant atoms, this means pairing to a defect that is stationary relative to the degree of mobility that the TM has in the unpaired state. The time an ionized TM spends paired to a dopant atom reduces the aggregate mobility of the TM in solution. The reaction such as that in equation 2.13 will have an equilibrium constant associated with it for a given T, $[Fe_i]_{tot}$ and $[A_s]$. The net eqilibrium constant is the balance between the rate of capture of mobile Fe_i^+ and release rate of paired Fe_i^+ and has been measuredby Kimerling *et al.* [35] others to have E_B values of 0.65eV and 0.58eV respectively.

$$D_{eff} = D_o(1 - f_{pr}) \tag{2.22}$$

where f_{pr} is the fraction of paired TM. We calculate f_{pr} based on the equilibrium constant for the pairing reaction for various p-type doping levels as a function of temperature and present the results in figure 2-9. Figure 2-10 shows the effect that the pairing has on D_{eff} for Fe_i for various p-type doping concentrations.

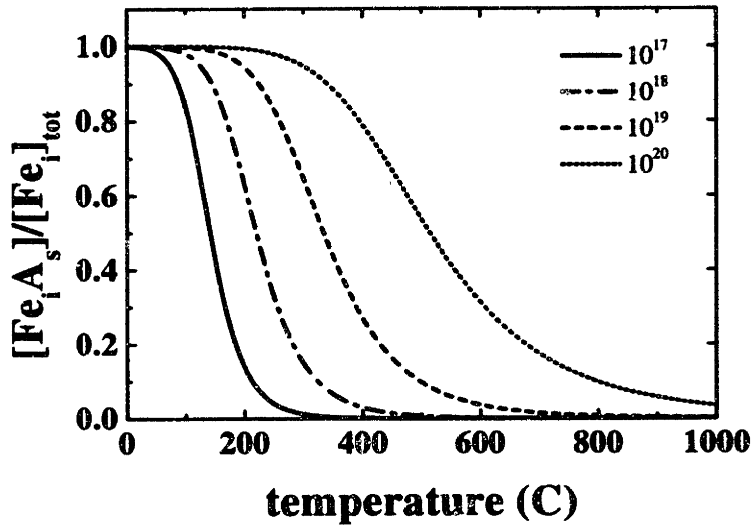

Figure 2-9: Fraction of paired Fe$_i$ of the total Fe$_i$ content as a function of temperature for various doping levels per cm^3.

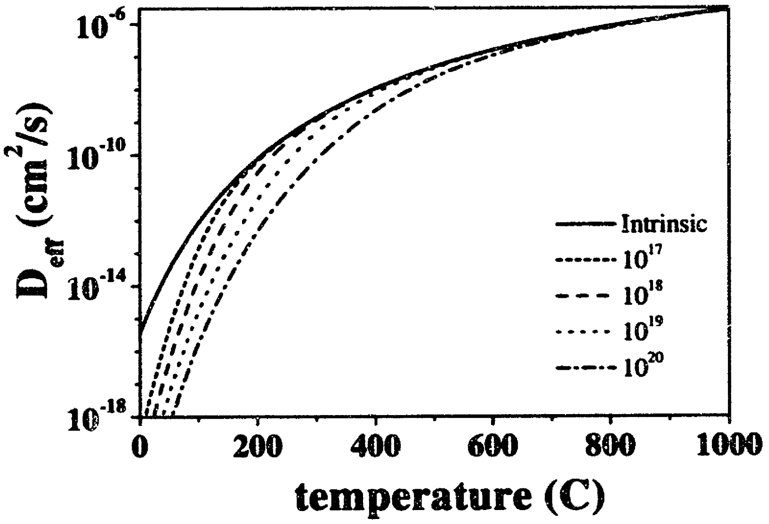

Figure 2-10: Calculation of D_{eff} for Fe$_i$ in Si as a function of temperature for various degrees of p-type doping per cm^3. The diffusivity of Fe$_i$ in intrinsic Si is also presented for comparison.

The high temperature D_{eff} collapses to the intrinsic case due to the instability of the pairs as the thermal energy becomes significant compared to E_B, but in the lower temperatures and the more heavily doped Si, the effect of pairing on D_{eff} is pronounced.

While we have focused our attention on the results for the case of Fe in Si, the analysis can be applied to any transition metal provided the degree of ionization and E_B are known.

Chapter 3

Solubility Driven Redistribution

3.1 Segregation Driven by Doping Variation

As described in Subsection 2.1.2, p-type dopants increase the solubility limit for donor defects such as Fe, Cu, and Ni. Another way to describe dopant induced solubility enhancement is that the presence of dopants lowers the chemical potential for the TM defect in the doped region. Since mass transport is driven by a gradient in chemical potential, we see that regions of different doping with initially equal TM defect concentrations will redistribute their impurities until the gradient in chemical potential is eliminated.

Since we are interested in modeling the contaminant redistribution based on the driving force for redistribution, it is useful to define a segregation coefficient for a species X, $k_X^{p/i}$, between differently doped silicon regions:

$$k_X^{p/i} = \frac{C_{sol}^p(X)}{C_{sol}^i(X)} \tag{3.1}$$

where $C_{sol}^p(X)$ and $C_{sol}^i(X)$ are the solubility limits of species X in the p-doped and intrinsic Si regions, respectively. We are familiar with the idea of a segregation coefficient for a trace impurity between the liquid and solid phase of a material. We might, for example, have used such an impurity segregation coefficient to estimate the degree of impurity rejection during a process such as Si crystal growth. The

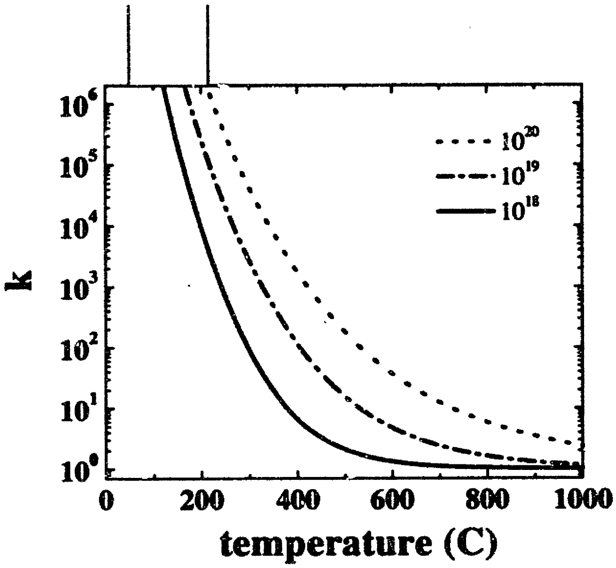

Figure 3-1: Segregation coefficient, $k_{Fe}^{p/i}$ as a function of temperature for various degrees of high p-type doping as described in Smith *et al.*

segregation coefficient between doped and undoped Si, $k_X^{p/i}$, is just the ternary analog to the binary system segregation coefficient.

3.2 Segregation to Molten Aluminum

The success of the solar cell industry demands production of a high efficiency device with input costs as low as possible, and unlike the integrated circuit industry, the competition is not against other device manufactures, but against other means of producing electricity. This market reality necessitates strict cost constraints on the manufacturing processes. In silicon based PV manufacture, the need to keep costs down makes the use of lower grade silicon feedstock material and compromises on the clean processing environment commonplace. Maximizing cell efficiency for minimal cost requires optimizing processes to maximize their effect at controlling the inevitable transition metal contaminants.

Al alloyed back contacts are known to improve solar cell device performance due

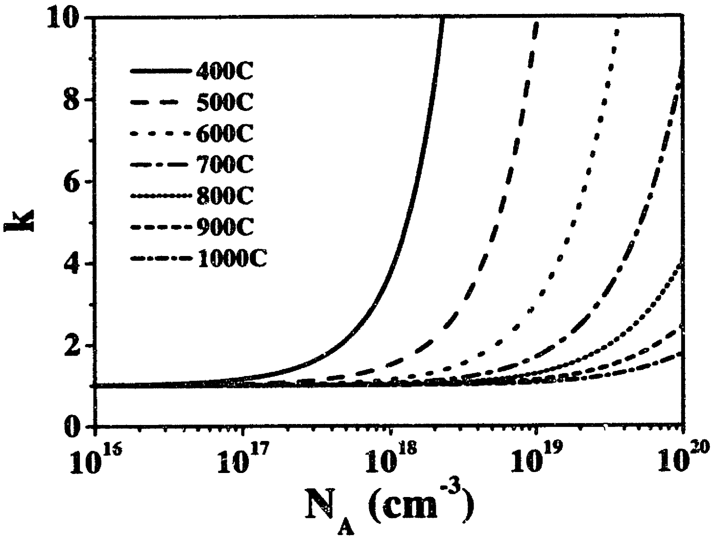

Figure 3-2: Calculation of the segregation coefficient, $k_{Fe}^{p/i}$ as a function of acceptor concentration for various temperatures. $k_{p/i}^{Fe}$ goes to unity as temperatures beyond the extrinsic regime are reached.

to the generation of a heavily p-doped region on the p-type substrate. The heavy doping serves to cause band bending such that minority carriers are repelled from the back surface and surface recombination is significantly reduced. At the same time, the high solubility for transition metals in the Al-Si molten alloy allows for segregation to the back contact region from the bulk of the device. Most manufacturers use Al back surface contacts on their silicon PV devices. We are interested in quantitatively characterizing and simulating this gettering effect to guide process optimization for gettering. In general, device process conditions are dictated by the electrical requirements, but if sufficient understanding of the gettering effect can be transformed into device efficiency improvement or if processes can be tuned within the constraints governed by the device design constraints, then material quality improvements can be maximized.

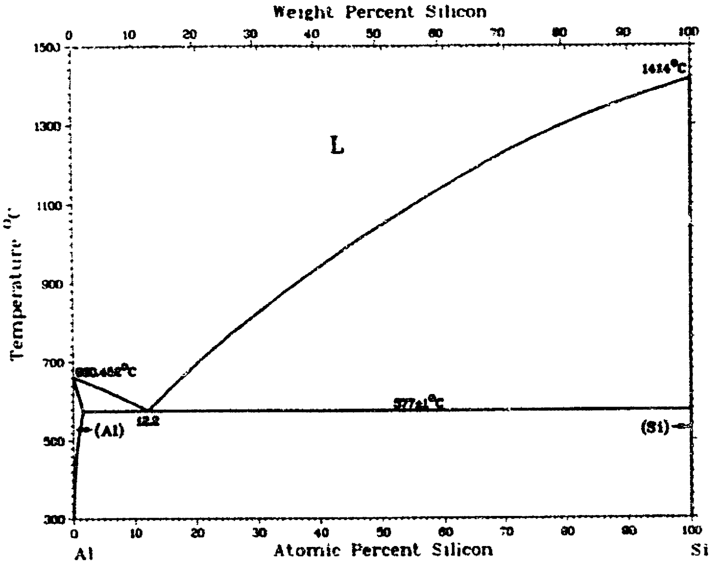

Figure 3-3: Al-Si binary phase diagram from Massalski *et al.* [41].

3.2.1 Thermodynamics

We use the Thermo-Calc generated ternary phase diagram for Al-Fe-Si together with the dopant enhanced solubility model to calculate the segregation coefficient, $k_{Fe}^{L/\alpha}$ for Fe between the Al-Si alloyed contact region, or the liquid phase denoted by L, and the silicon matrix, or the Si solid solution denoted by α, at processing temperatures in order to quantitatively estimate the gettering capacity of Al back contact formation.

In figure 3-3 we present the Al-Si binary phase diagram. The Al-Si system is a simple eutectic with eutectic temperature of 577°C. The solidus line for the α phase is not visible on this scale as the solid solubility for Al in α is on the order of parts per ten thousand. The Fe-Si phase diagram. figure 3-4, is much more complicated, but again, the α solidus line is on the pure Si axis for this scale.

We extrapolate the ternary phase diagram from the three binary phase diagrams as in Calphad by Kaufman [37, 38]. Using the regular solution model, interaction parameters were introduced to allow for finite solubility of Al and Fe in α subject to

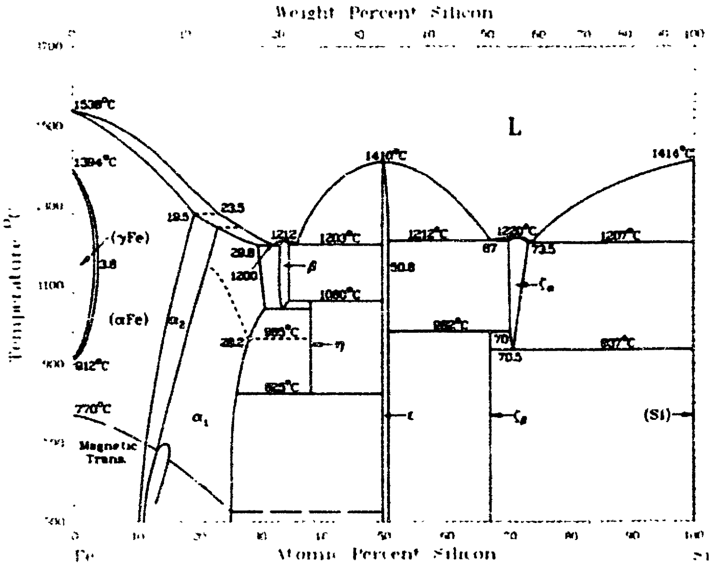

Figure 3-4: Fe-Si binary phase diagram from Massalski *et al.* [41].

the known solid solubility limits for each of the dilute species. We made modifications to allow for finite solubilities of the third component in binary compounds in order to generate the ternaries. Thermo-Calc [39, 40] is a software package that implements the Calphad method with a convenient user interface. Thermodynamic data bases are included in the Thermo-Calc software, but customization made data bases are easy to incorporate. The data base generated for this work is included in appendix

Once the Al-Fe-Si ternary phase diagram has been generated, we can then examine isothermal slices of the ternary diagram to model the Al-Si alloy liquidus line as a function of temperature. For isothermal slices at 600°C, 650°C, 700°C, 800°C, 900°C and 1000°C, the eutectic liquidus is reasonably approximated by a line with slope approximately constant in temperature. Figure 3-5 shows a schematic isothermal slice with the construction used to estimate the slope of the liquidus line or, in other words, the ratio in change in Fe mole fraction to change in Al mole fraction. We also note the intercept of the liquidus line with the Al-Si binary axis, $(x_{Al}^L)_{int}$, and the Al mole fraction of the other end point of the liquidus line, $(x_{Al}^L)_{min}$. We can now solve

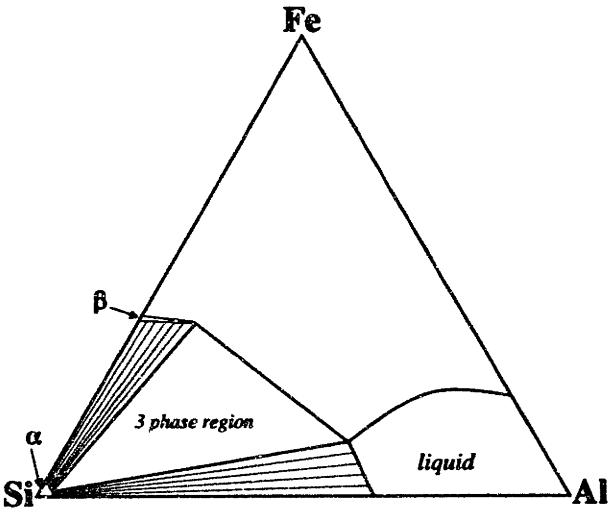

Figure 3-5: Schematic of an isothermal slice of the Al-Fe-Si ternary phase diagram above the eutectic temperature.

for the maximum mole fraction of Fe in the Al-Si liquid to define one boundary for the two phase region between Si solid and the Al-Si eutectic alloy.

We then estimate the Fe solid solubility in silicon for the case of aluminum at the solubility limit using the dopant enhanced solubility model described in subsection 2.1.2 to define the solidus boundary of the two phase region. We then determine $k_{Fe}^{L/\alpha}$ by taking the ratio of the maximum mol fractions for Fe in the liquid, $(x_{Fe}^{L})_{max}$ and that in Si solid phase $(x_{Fe}^{\alpha})_{max}$. Figure 3-6 shows the calculated segregation coefficient between the Al-Si eutectic liquid and solid silicon from the eutectic temperature to 1000°C.

3.2.2 Kinetics

Now that we have established a model for the thermodynamic driving force for redistribution of Fe from the Si solid solution to the Al-Si molten alloy during a high temperature gettering process with Al alloyed back contacts, we would like to appropriately model the kinetic response to this driving force. We want to solve for the flux

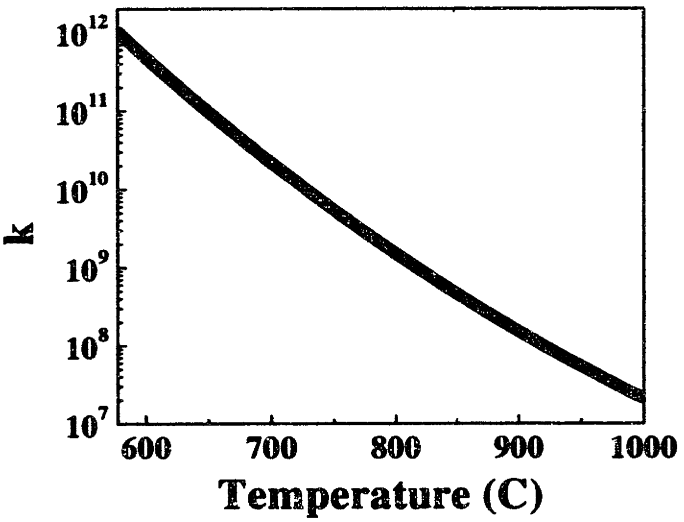

Figure 3-6: Calculation of the the segregation coefficient, $k_{Fe}^{L/\alpha}$, for Fe in Al-Si eutectic liquid relative to the Si solid solution as a function of temperature.

Figure 3-7: Schematic diagram for the interface between α and Al-Si eutectic liquid phases.

crossing the interface from one phase to the other for a given concentration profile in each phase. There will be an activation barrier, ΔG^*, between the Si solid and the Al-Si alloy liquid. We can employ reaction rate theory and transition rate theory to get the non-equilibrium thermodynamic response to a finite chemical potential difference at the $\alpha - L$ interface.

The segregation coefficient is defined as follows:

$$k_{Fe}^{L/\alpha} = \frac{C_{sol}^{L}(Fe)}{C_{sol}^{\alpha}(Fe)} \tag{3.2}$$

where $C_{sol}^{L}(Fe)$ and $C_{sol}^{\alpha}(Fe)$ are the Fe solubility limits in the L and α phases respectively. Since the overall levels of Fe coming into play in this system are very low, the

Figure 3-8: Schematic representation of the activation barrier, ΔG^*, for migration of Fe atoms across the α-L boundary.

dilute solution conditions apply and we can model the chemical potential for Fe in Si and for Fe in the Al-Si alloy as being Henrian. The chemical potential is then directly proportional to the natural logarithm of the concentration with equation (3.3)

$$\mu^{\alpha}_{Fe} = \mu^{o}_{Fe}{}^{(\alpha)} + k_B T \ln \gamma_\alpha + k_B T \ln x^{\alpha}_{Fe} \tag{3.3}$$

$$\mu^{L}_{Fe} = \mu^{o}_{Fe}{}^{(L)} + k_B T \ln \gamma_L + k_B T \ln x^{L}_{Fe} \tag{3.4}$$

To represent the segregation coefficient in terms of the chemical potential we solve for the difference in chemical potentials of Fe in the respective phases:

$$\Delta\mu^{L\to\alpha}_{Fe} = \left(\mu^{o}_{Fe}{}^{(L)} + k_B T \ln(\gamma_L x^{L}_{Fe})\right) - \left(\mu^{o}_{Fe}{}^{(\alpha)} + k_B T \ln(\gamma_\alpha x^{\alpha}_{Fe})\right) \tag{3.5}$$

In equilibrium, $\Delta\mu^{L\to\alpha}_{Fe}$ is zero, giving:

$$\frac{x^{L}_{Fe}}{x^{\alpha}_{Fe}} = \frac{C^{L}_{sol}(Fe)}{C^{\alpha}_{sol}(Fe)} = \frac{\gamma_\alpha}{\gamma_L} \exp\left(-\frac{(\mu^{o}_{Fe}{}^{(L)} - \mu^{o}_{Fe}{}^{(\alpha)})}{k_B T}\right) \tag{3.6}$$

comparing with the definition of $k^{L/\alpha}_{Fe}$, we now have an expression for $\Delta\mu_{Fe}$ in terms of non-equilibrium concentrations of Fe in the respective L and α phases, $C^{L}_{sol}(Fe)$ and $C^{\alpha}_{sol}(Fe)$, and the calculated segregation coefficient for the system, $k^{L/\alpha}_{Fe}$:

$$\Delta\mu^{L\to\alpha}_{Fe} = k_B T \ln\left(\frac{C^{L}(Fe)}{k^{L/\alpha}_{Fe} C^{\alpha}(Fe)}\right) \tag{3.7}$$

When simulating diffusion, we use concentration based equations such as Fick's law to model the mass transport responding to gradients in concentration, but when we examine inhomogeneous media, we need to derive the boundary conditions from the more fundamental response of matter flux to the chemical potential gradient created by the presence of that interface.

$$\vec{J} = -L\vec{\nabla}\mu \tag{3.8}$$

where $\vec{J}$ is the flux of the chemical species, μ is the spatial function of the chemical potential of that species and L is the coupling term. The negative sign is due to the fact that systems proceed toward equilibrium or zero gradient in chemical potential to maximize entropy in accordance with the second law of thermodynamics. The flux of the chemical species must flow in such a way as to damp out the existing gradient in chemical potential.

In the Henrian approximation, the flux equation can be put in terms of concentration:

$$\vec{\nabla}\mu = \frac{k_B T}{C}\vec{\nabla}C \tag{3.9}$$

$$\vec{J} = -L\left(\frac{k_B T}{C}\vec{\nabla}C\right) \tag{3.10}$$

Mobility, M, is defined as relating an aggregate particle velocity, $\vec{v}$, to a chemical potential gradient.

$$\vec{v} = -M\vec{\nabla}\mu = -M\left(\frac{k_B T}{C}\vec{\nabla}C\right) \tag{3.11}$$

A drift flux can be written in terms of $\vec{v}$:

$$\vec{J} = \vec{v}C = -Mk_B T\vec{\nabla}C \tag{3.12}$$

Comparing equations (3.10) and (3.12), determines L

$$L = MC \tag{3.13}$$

Comparing (3.12) with Fick's First Law:

$$\vec{J} = -D\vec{\nabla}C \tag{3.14}$$

produces the Nearst-Einstein Equation:

$$D = Mk_BT \tag{3.15}$$

Now we examine the reaction rate kinetics across the interface. We know that the flux across the interface is conserved and that gives us the following relation:

$$D^L_{Fe}\frac{\partial C^L_{Fe}}{\partial x}\bigg|_{x=x_o} = D^\alpha_{Fe}\frac{\partial C^\alpha_{Fe}}{\partial x}\bigg|_{x=x_o} \tag{3.16}$$

where x_o is the position of the α-L interface and D^L_{Fe} and D^α_{Fe} are the diffusivities of Fe in the L and α phases respectively.

We can also set up a net flux equation by examining the change in concentration on the L side of the interface as follows:

$$\vec{J} = \lambda\frac{dC^L_{Fe}}{dt} = \lambda\left(k^+(C^\alpha_{Fe})_{x=x_o} - k^-(C^L_{Fe})_{x=x_o}\right) \tag{3.17}$$

where λ is the jump distance across the interface, some average of the atomic spacing in the Si matrix and the molten Al-Si alloy, C^α_{Fe} and C^L_{Fe} represent the Fe concentrations at the edge of the Si and Al-Si alloy regions respectively, and k^+ and k^- represent the probability per unit time of successful jumps from the α phase to the L phase and from the L phase to the α phase respectively. k^+ and k^- can be determined by transition rate theory according to the analysis of Vineyard [43].

$$k^+ = \frac{k_BT}{h}\exp\left(-\frac{(G^* - G^\alpha)}{k_BT}\right) \tag{3.18}$$

$$k^- = \frac{k_BT}{h}\exp\left(-\frac{(G^* - G^L)}{k_BT}\right) \tag{3.19}$$

where G^α and G^L are the Free Energies for Fe in the α and L phases respectively. In equilibrium, the forward flux will equal the reverse:

$$k^{+}(C_{Fe}^{\alpha})^{eq} = k^{-}(C_{Fe}^{L})^{eq} \tag{3.20}$$

giving:

$$\frac{k^{+}}{k^{-}} = \frac{(C_{Fe}^{L})^{eq}}{(C_{Fe}^{\alpha})^{eq}} = k_{Fe}^{L/\alpha} \tag{3.21}$$

and rewriting with equation (3.7) gives:

$$k^{-} = \frac{k^{+}}{k_{Fe}^{L/\alpha}} \tag{3.22}$$

We can then substitute into the interface flux condition, (3.17) and simplify:

$$\vec{J} = \lambda k^{+}\left(C_{Fe}^{\alpha} - \frac{C^{L}}{k_{Fe}^{L/\alpha}}\right) \tag{3.23}$$

k^{+} as described in (3.18) represents the probability of a successful jump of an interstitial Fe atom from the α phase to the L phase.

$$\vec{J} = \frac{D_{int}}{\lambda}\left(C_{Fe}^{\alpha} - \frac{C_{Fe}^{L}}{k_{Fe}^{L/\alpha}}\right) \tag{3.24}$$

One further complication with simulating the $\alpha - L$ boundary is that the segregation coefficient, $k_{Fe}^{L/\alpha}$, was defined relative to the $(C_{Fe}^{\alpha})^{eq}$ at the particular temperature for Si doped at the solid solubility limit for that temperature. The indiffusion of aluminum into the Si solid is extremely slow, so to a good approximation, the wafer will retain its original p-type doping level. At temperatures above 900°C, this should be relatively unimportant as the segregation coefficient between Si regions of different p-type doping goes to unity. At lower temperatures or for extremes in the difference between the actual doping level and that of a wafer doped to the solid solubility limit at the alloying temperature of interest, we need to adjust the segregation coefficient. In (3.7) we have a relation for $\Delta\mu$ between the Al alloy layer and the Si solid. Earlier, we have developed a model for the segregation coefficient of Fe between p-type doped Si and intrinsic Si, k_{Si}. That model can then be used to generate a $\Delta\mu$ between Si p-doped at the solubility limit and the actual doping level present:

$$\Delta\mu^{p_{sol}\to p} = k_B T \ln\left(\frac{k_{Fe}^{p/i}(C_{Fe}^{\alpha})_{p_{sol}/i}}{k_{Fe}^{p_{sol}}(C_{Fe}^{\alpha})_p}\right) \tag{3.25}$$

Combining with equation (3.7) gives the total chemical potential difference between the generally doped p-type Si α phase and L.

Now we can model the driving force for Fe redistribution between a Si region of any doping level and the molten Al-Si alloy layer in Al back contact formation.

$$\vec{J} = \frac{D_{int}}{\lambda}\left(C_{Fe}^{p} - \frac{k_{Fe}^{p/1}C_{Fe}^{L}}{k_{Fe}^{p_{sol}/i}k_{Fe}^{L/\alpha}}\right) \tag{3.26}$$

While we have reasonable methods of modeling the various segregation coefficients in in equation 3.26, we know very little about what an appropriate choice for D_{int} should be.

Chapter 4

Precipitation Gettering

In the last chapter, we looked at the role of TM redistribution from one phase or region of the wafer to another on impurity gettering. In lightly contaminated material, these segregation gettering mechanisms are the only ones that are operating. When wafers are heavily contaminated, supersaturation at the gettering temperature will create a driving force for removal of supersaturated metals via silicide precipitate formation in the wafer. The IC industry routinely uses intentionally created heterogeneous nucleation sites, or Internal gettering (IG) sites, within the wafer to promote precipitation away from the wafer surface. In the manufacture of photovoltaics, the wafer bulk is the active region of the device, making silicide precipitation a less desirable option to gettering to an external phase. As discussed earlier, equation 1.3 shows that between the option of fewer aggregated impurities as opposed to a significantly larger number of dispersed TM defects, the aggregation is desirable so long as the precipitate does not have a significantly larger minority carrier capture coefficient compared to that of the isolated defect. For the solar cell application, we would like to know as much as possible about metal-silicide nucleation so that we can frustrate it in favor of external gettering methods.

4.1 Internal Gettering

In the IC industry, the predominant substrate is Czochralski grown (Cz) dislocation free Si. The Cz growth process generates high levels of oxygen supersaturation due to the dissolution of the quartz crucible over the course of growth and the segregation coefficient for O toward redistribution into the solid relative to the melt. Growth techniques have been developed that significantly reduce the incorporation of O into the Si crystal during growth, but the excess O has been found to be beneficial for both gettering [45, 46] and mechanical resistance to thermal stress [47, 48]. The IC industry uses a well known high-low-high heat treatment to convert the as-grown excess O concentration into the desired profile of IG sites. The first high temperature step serves to outdiffuse excess O from the near surface region. This step will define a region free of IG sites to prevent strain and other defects from affecting the device region. It is typically carried out at temperatures above 1100°C in an inert ambient. The duration of the treatment will determine the width of the defect free region, which is referred to as the denuded zone (DZ). The low temperature heat treatment step is carried out in the 600-750°C regime to create large undercooling relative to the [O] promoting appreciable nucleation of SiO_2. The last step is a high temperature treatment (1000-1100°C) to expedite SiO_2 precipitate growth. IG sites are formed by nucleation and growth of SiO_2 precipitates and their associated dislocations and stacking faults, see for example the review by [49]. The presence of these aggregates of Si self-interstitials (I) and the observation of retardation of SiO_2 precipitate growth during oxidation of the surfaces has led to the acceptance of the concept that SiO_2 precipitate growth is coupled to the concentration of I. The governing reaction was proposed by Hu [50]

$$2xO_i + ySi_s \rightleftharpoons xSiO_2 + (y-x)Si_i \tag{4.1}$$

The stoichiometric coefficients account for the fact that the specific volume, or the volume per Si atom, of SiO_2 is roughly 2.25 times that of Si. Precipitation will produce strain as well as the emission of I. Supersaturation of I will result in the condensation of these point defects into aggregates, particularly during cooling from a high temperature growth step. The punched out dislocation loops and stacking faults are evidence of the role of the I point defect in SiO_2 precipitation.

4.2 Metal Silicide Growth

Researchers have been monitoring the precipitation processes of TM-silicides in silicon for many decades. Harmful TM contaminants are known to heterogeneously nucleate at IG sites. Heterogeneous nucleation implies a very low barrier to nucleation. The expectation therefor, is that TM precipitation at these sites will exhibit diffusion limited kinetics. Researchers have demonstrated this to be true, most quantitatively for the case of Fe where Gilles *et al.* [51] were the first to apply Ham's Law [52] to successfully model IG gettering kinetics.

The rate of precipitation to IG sites in the model is inversely proportional to the product of the IG site density, N_{IG} times the IG site effective radius, R_{IG}. When this product is increased, the equilibration time will decrease. The time constant for internal gettering, τ_{IG}, scales as follows

$$\tau_{IG} = \frac{1}{4\pi N_{IG} R_{IG} D_{eff}} \tag{4.2}$$

Heterogeneous nucleation is typically faster than homogeneous nucleation due to the smaller barrier, but homogeneous nucleation is observed for the fasted diffusing TM.

The appearance of haze, or near surface precipitates generated during relatively rapid cooling and then revealed by selective etching, has been used as a test for metal contamination. Some metals, Cu, Ni, Pd and Co, and Fe under very specific circumstances also have the ability to form homogeneous silicide precipitates in the bulk of the wafer. The homogeneous nucleation rate and precipitate morphology are intimately connected to the silicide phase formed. Nucleation and growth processes in a supersaturated phase are driven by the reduction in free energy, Δg_v, gained by forming a new solute-rich phase less the interfacial energy, γ, and strain energy, Δg_s, caused by accommodating the new phase in the host matrix.

$$\Delta G = 4\pi r^2 \gamma + \frac{4}{3}\pi r^3 (\Delta g_s - \Delta g_v) \tag{4.3}$$

Assuming a spherical precipitate of radius r. The presence of haze, or near surface precipitates, provides strong evidence that growth becomes point defect diffusion limited at some point. Just as in the case of SiO_2 precipitation, the specific volumes that need to be accommodated for most silicides will produce significant Δg_s. Emission of I or absorption of V will allow some degree of relation of Δg_s. For cases where the specific volume of the silicide is smaller that that of the Si solid, emission of V is required to relieve strain energy. Since the wafer surface acts as a sink for excess point defects, precipitates near the surface will have the fastest growth rate. As discussed in section 2.1, the TM solid solubility limit is determined by the common tangent construction on $G_\alpha^{eq}(x)$ and $G_\beta^{eq}(x)$, the equilibrium Gibbs Free energy curves of the α and metal silicide phases respectively. When the silicide phase is strained, $G'_\beta(x)$ is raised, shifting the common tangent curve and increasing x_{sl} as represented schematically in figure 4-1. An increase in x_{sl} is equivalent to a reduction in driving force for silicide precipitate growth. If the strain energy can be relaxed by the emission of I, $G'_\beta(x)$ will drop towards $G_\beta^{eq}(x)$ and the driving force for silicide growth will increase. When I accumulate in the Si matrix near the precipitate, further I emission is suppressed and the driving force for silicide growth is again reduced. I emission or I diffusion will become rate limiting for precipitate growth. The case of silicides with a specific volume lower than Si is the same except the rate limiting point defect is the V. Emission of V or absorption of I will allow relaxation of the tensile strain that accumulates as the precipitate grows.

Why the point defect mediated means of relieving strain is needed for homogeneous precipitates, after significant growth, precipitates that begin forming at heterogeneous sites could also run out of defect sources or sinks and the initiating site. Experimental results demonstrate that for lower temperatures Fe gettering data with Al coated surfaces, we do leave a fast gettering regime with Fe diffusion limited kinetics and

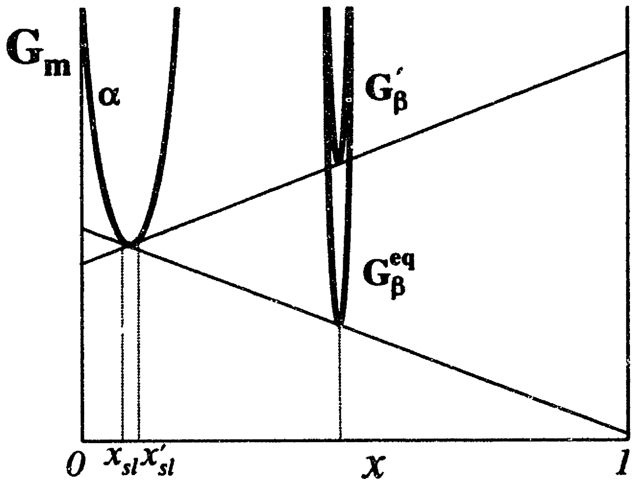

Figure 4-1: Common tangent construction demonstrates how Δg_s increases x_{sl} and reduces the driving force for silicide phase growth.

gradually shift to a regime dominated by a slower process. These data will be address in more detail in chapter 6.

Chapter 5

Simulation to Model Processing

Gettering was first described by Seidel as consisting of three steps: impurity release from the region where is has a deleterious impact, transport of the impurity to a region of state where its impact is benign, and successful irreversible capture at the benign gettering site [44]. A process model enables examination of the interactions of the wafer design parameters, the process parameters, the thermodynamic driving forces, and the kinetic limitations for gettering. The wafer parameters, as defined above, include substrate doping level, N_A, initial contamination concentration, and the properties of the oxygen precipitate distribution in the system such as the denuded zone (d_{DZ}) width, the oxide precipitate density, N_{IG}, and the effective radius of the precipitates, R_{IG}. In addition to the d_{DZ} width, wafer thickness and epilayer thickness are important length parameters of the system. Any back-surface treatment must be parameterized in terms of IG site density and effective site radius. Figure 5-1 shows a schematic wafer design with the various parameters included.

5.1 Trends for Gettering Mechanisms

In a broad sense, device processing causes temperature variations, doping level and type changes, perturbations of equilibrium native point defect concentrations, introduction of surface stress and exposure to undesired contaminants. Fe in p-type silicon is an interstitial defect. Neglecting induced surface stress, the dominant impacts of

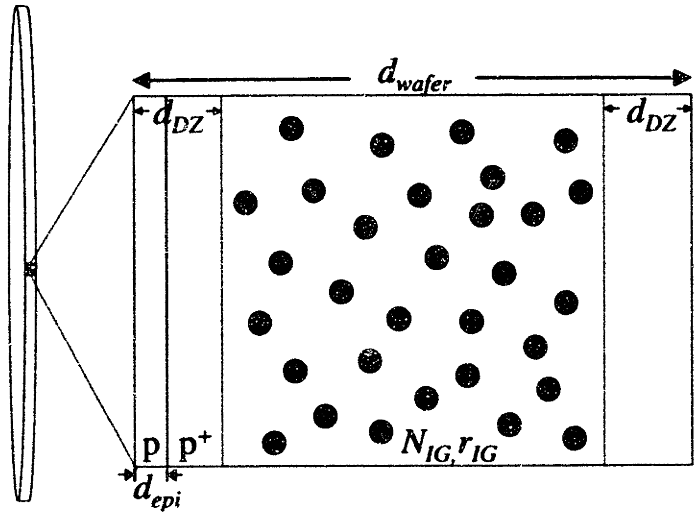

Figure 5-1: The various parameters for an epitaxial p on p^+ wafer with IG sites.

processing on Fe redistribution in p-type silicon are through thermal treatments and additional Fe introduction from the wafer surfaces. While any modeling software is easily adaptable to exploring any generalized time-temperature profile, we focus on constant temperature and linear cooling to reveal the fundamental thermodynamic and kinetic trends of the system. Constant temperature anneals of appropriate duration reveal thermodynamic properties of the system. A constant temperature cool examines both an inevitable processing step, i.e. returning to room temperature, and the dominating kinetics at the various temperature regimes. Initial contamination levels are varied to examine the role of supersaturation and undersaturation in the Fe redistribution kinetics.

Internal gettering mechanisms considered here include internal gettering at heterogeneous nucleation sites presented by intentionally or unintentionally created SiO_2 precipitates in the wafer bulk and gettering associated with heterogeneous nucleation at sites generated by a wafer back surface treatment, such as back surface damage or polysilicon growth. In this model, we assume contaminant precipitation at oxide or damage sites is diffusion limited and driven by supersaturation and that the sites can be parameterized by an effective radius, R_{IG}, and density, N_{IG} that captures the gettering effect of a wafer treatment. The governing equation is as follows:

$$\frac{\partial C(x,t)}{\partial t} = D_{eff}\frac{\partial^2 C(x,t)}{\partial x^2} + 4\pi D_{eff} N_{IG} R_{IG}(C_s - C(x,t)) \tag{5.1}$$

after Tan *et al.* [53] where C(x,t) is concentration of Fe_i, and D_{eff} is the effective diffusivity of Fe. Equation 5.1 represents a mean field model that assumes simplified, spherical heterogeneous nucleation sites for contaminant precipitation. Equation 5.1 allows for both the precipitation of Fe_i when the contamination level exceeds the solubility limit and for the dissolution of Fe_i from precipitates when the background contamination level drops below the solubility limit. The specific nature of the IG site will affect the kinetics of internal gettering. The details of how the IG site facilitates heterogeneous nucleation, whether via the oxide/silicon interface or by punching out dislocations which then serve as sites, will determine the most accurate quantitative approach toward modeling internal gettering. In the current model, the IG sites are assumed to be spherical precipitates that serve as heterogeneous nucleation sites for silicide precipitation. The model algorithm updates the radius of these precipitates by assuming a spherical cap of silicide around the initial oxide precipitate. The assumption of diffusion limited precipitation kinetics is reasonable based on experimental observations [55]. The experimental result of an initial exponential decay of [Fe_i] due to IG sites confirms the basic assumptions of the model.

Using the principles outlined above, we have developed a numerical model to calculate the redistribution of Fe for various wafer designs, processing conditions and contamination levels. The results allow determination of the engineering tradeoffs for effective gettering. We use finite difference diffusion calculations to follow the redistribution of Fe between a thin lightly doped epilayer and a thick p^+ substrate. Flux at the epilayer/substrate interface between the lightly doped epitaxial layer and the heavily doped substrate, $F(p/p^+)$, is given by Antoniodis and Dutton [56]:

$$F(p/p^+) = \frac{D_{eff}}{\Delta x}\left(\frac{(C_{p^+}(x+\Delta x)}{k_{p^+/p}} - C_p(x)\right) \tag{5.2}$$

$C_{p^+}(x+\Delta x)$ is the concentration of Fe_i at the interface in the heavily doped substrate region; $C_p(x)$ is the concentration of Fe_i at the interface in the lightly doped epilayer; k is the segregation coefficient of the heavily doped region with respect to the lightly doped region; and Δx is the grid size. We use an implicit Crank-Nicholson method and compute mass conservation to determine a maximum time step for each contaminant. Unless explicitly stated, such as with the case of BSD, external boundaries are assumed to be perfectly reflecting.

While it is well understood that near surface contamination removal is dependent on i.) mass transport from the near surface, or diffusion, ii.) precipitation at some site away from the device region, and iii.) segregation from the device region, the exact role of each of these determines wafer and process design for gettering. We present a conceptual framework to capture the role that each of these mechanisms plays in enabling gettering for the particular case of Fe. With appropriate data, the understanding developed here can be easily generalized to any transition metal impurity.

Contaminant redistribution requires both a gradient in chemical potential and mobility of the species to be gettered. As mentioned above, the diffusivity of Fe in p-type silicon is a function of both temperature and doping level. A common length scale for diffusion is the characteristic diffusion length, L_D, given by Equation 5.3.

$$L_D = C_1 (D_{eff} t)^{1/2} \tag{5.3}$$

where t is diffusion time, and the scaling factor, C_1, will depend on the dimensionality of the diffusion and the particular profile under study. The effective diffusivity is a function of N_A and temperature. From equation 5.3, we can calculate the time for appreciable diffusion to the back surface of the wafer to estimate the effectiveness of back surface treatments for a heat treatment of a particular duration of time. However, it should be noted that this metric offers no conclusions about the role that back surface poly can play in reducing contaminant introduction from the backside of the wafer during processing. We can also use equation 5.3 to estimate the time required for transport from the front surface across the denuded zone width to the IG sites. The estimates in both cases will be coarse, however, for the following reason. Equation 5.3 describes diffusion from an error function or delta function distribution over time. For the error function, L_D represents indiffusion from a surface and it measures the depth of the concentration of 1/e times the surface concentration. For the case of a delta-function initial concentration profile, a Gaussian function describes the evolution of the concentration profile with L_D representing the FWHM value for the profile. The reason for revisiting these details is to emphasize the fact that a characteristic length scale for mass transport is inherently tied to a particular gradient in chemical potential. Thus, alterations in the gradient of chemical potential, as well as the initial contamination profile, can serve to either enhance or reduce mass transport.

Internal gettering is driven by supersaturation of contaminants at a given process temperature and is enabled by mobility and mass transport of the species. Internal gettering sites serve as centers for heterogeneous nucleation of contaminant precipitates which consume the contaminants from solid solution. At higher temperature, for a given contaminant concentration, the kinetics allow for rapid equilibration, but the solubility limit is also high, resulting in limited impurity reduction. For a low temperature thermal treatment, the supersaturation will be much greater, but the rate of reaching equilibrium solubility will be slow due to reduced mobility.

For the case of indiffusion of Fe from the lightly doped surface of an epitaxial wafer with a heavily doped substrate, segregation will act to drive mass transport of Fe into the wafer away from the surface. For the case of uniform contamination, such as contamination introduced during (crystal) growth, segregation at an interface is an effect that contributes to Fe redistribution from an epilayer to the heavily doped substrate. However, both constant temperature annealing and slow cooling reveal that segregation gettering as the sole gettering mechanism is not very effective. This can be understood by the fact that the gettering capacity of the heavily doped substrate with respect to the epilayer is finite. At high temperatures where redistribution to equilibrium is rapidly accomplished, k is near unity. At lower temperatures where k is significantly large, the time scale required to access the gettering capacity of a several hundred micrometer thick wafer are prohibitive. These factors serve to make the gettering effectiveness of only segregation by doping enhanced solubility small except for those contaminants that diffuse very rapidly at temperatures above 600°C.

In contrast, segregation in concert with internal gettering brings orders of magnitude improvement in Fe removal from the near surface region over IG gettering alone during slow cooling. This synergistic relationship between IG and segregation can be understood in terms of mass transport being driven by a gradient in chemical potential. On its own, segregation allows for some accumulation of Fe at the epilayer/substrate interface causing a gradient for redistribution to all reaches of the substrate. When internal gettering is present, k causes accumulation of Fe at the interface, but the IG sites across the denuded zone act to equilibrate the Fe concentration at the solubility limit. The supersaturation at one side of the denuded zone and rapid adjustment to saturation on the other serve to maintain a strong gradient which becomes stronger at lower temperatures as k and supersaturation. For enabling Fe redistribution from the near surface region, this gradient enhancement effect more than compensates for the reduction in mobility of Fe in highly doped silicon at lower temperatures. Another factor that will enhance the gradient is higher $N_{IG}R_{IG}$ product to insure rapid equilibration at the IG sites. Clearly, as contamination specifications drop further below the contamination solubility limit found at temperatures allowing for diffusion of Fe on reasonable time scales, the gradient and thereby the driving force for redistribution from the device region of the wafer will be reduced.

The significance of back surface damage in contamination removal from the wafer front surface is a function of wafer thickness, treatment time and temperature, and BSD gettering site density. The segregation ratio between back surface poly and single crystalline bulk is not known. However, under supersaturation conditions, it is clear that grain boundaries will serve as heterogeneous nucleation centers for contaminant precipitation. If no IG sites are present, BSD serves as the only sink for Fe in the system. When IG sites are available, BSD will only serve to accelerate the gettering process if the BSD site density is significantly higher than the IG site density. If this condition is satisfied, the equilibration rate at the back surface will be much higher than in the bulk, and a chemical gradient to the back surface will accelerate transport away from the front surface.

5.2 Interactions between Gettering Mechanisms

In Figure 5-2, we present the results for various wafer treatments on p/p$^+$ wafers where [A$_s$] in the epitaxial layer is 10^{15} cm^{-3}. The [A$_s$] in the p$^+$ substrate is set at 10^{19} cm^{-3}, and gettering is done at 700°C assuming a uniform initial Fe$_i$ contamination level. In the first case with no IG, Figure 5-2, we model a defect free, epitaxial wafer with no back surface damage. Fe$_i$ redistribution occurs; but the final concentration in the epilayer remains quite high, because there are no sinks for Fe in the system.

The next case, Figure 5-3, treats an epiwafer with intentionally enhanced oxygen precipitation and a denuded zone near the front and back surfaces. N_{IG} was 10^9 cm^{-3} with a precipitate radius of 20 nm in the IG region. The IG sites serve as the necessary sinks for reducing [Fe$_i$] in the system. These results demonstrate that segregation gettering from a lightly to a highly doped region is most effective when coupled with IG precipitation, and that BSD plays no role in gettering from the front surface in the case of Fe$_i$ under these conditions.

We explore an epitaxial wafer initially saturated with Fe at 1000°C cooling at a rate of 0.5°C/s. This slow cool rate amplifies the differences in wafer and process design by allowing time for the gettering to approach equilibrium. The rate of cooling from 1000°C to 300°C in around 20 minutes is a reasonable model for the air cooling rate of wafers as they are removed from from a tube furnace during batch processing.

Figure 5-4 plots the near surface [Fe$_i$] for three cases against the C_s (solid line) for the respective temperature at each point in the cool. The case where segregation is the only mechanism for gettering, the lack of sinks for Fe leave a high degree of supersaturated Fe$_i$ in the near surface region. In the case where IG sites are the only mechanism for gettering,the system is better able to equilibrate until the temperature

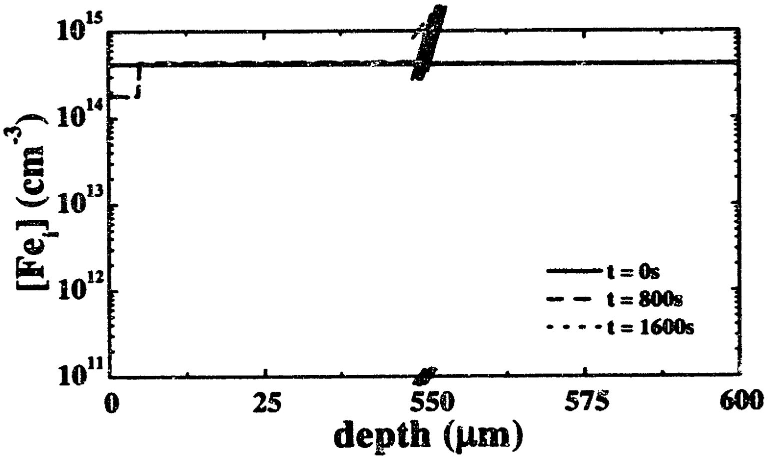

Figure 5-2: Simulation of a constant temperature heat treatment at 700°C after Fe contamination to the solubility limit at 1000°C on an epitaxial wafer that has no IG sites.

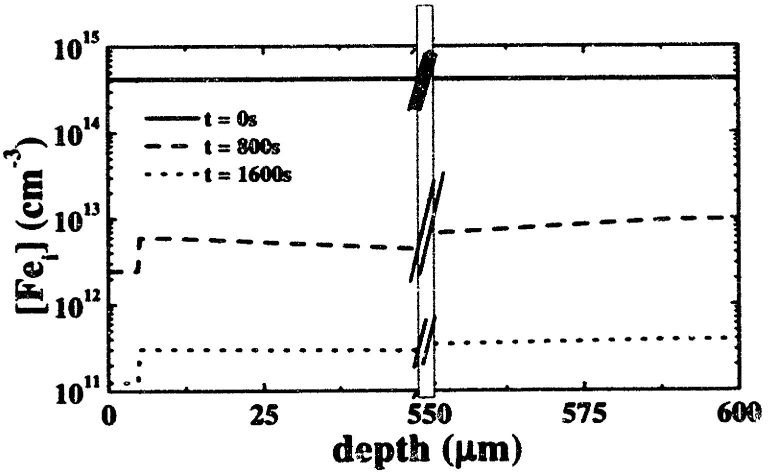

Figure 5-3: Simulation of a constant temperature heat treatment at 700°C after Fe contamination to the solubility limit at 1000°C on an epitaxial wafer that has an IG site density of 10^9 cm^{-3}.

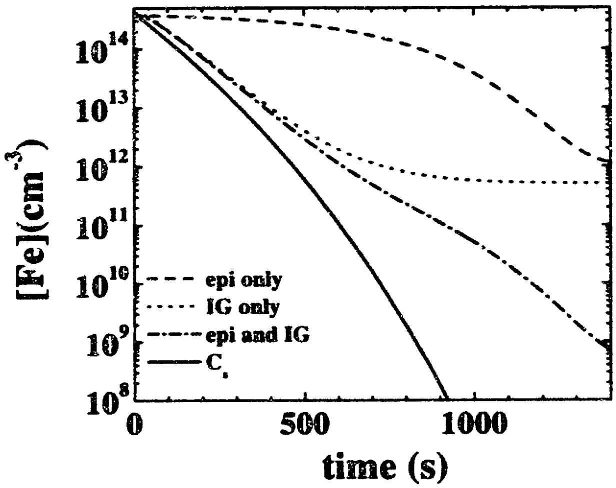

Figure 5-4: Simulation of a cool from 1000°C at 0.5°C/s for Fe contaminated wafers for the cases of segregation only, IG sites only, and both segregation and IG gettering. For the wafers with IG sites, N_{IG} is 10^9 cm^{-3}, R_{IG} is 20 nm, and the DZ width is 20 μm.

becomes too low for significant mass transport across the DZ to occur. The wafer DZ width is 20 μm, the IG site density is 10^9 cm^{-3}, with R_{IG} of 20 nm. We refer to this freeze out point as the DZ limit. In the final case of a lightly doped epilayer on a heavily doped substrate with identical IG site parameters, we see that significant gettering continues to occur beyond the DZ limit. The high temperature part of the cool is dominated by IG-controlled Fe precipitation from supersaturated solution as seen by the IG only curve, and the low T part of the cool is dominated by segregation due to the significant increase in k as T drops below 700°C. These results are consistent with the experiments for polished wafers. At $t > 800$ s, T is below 600°C; long-range diffusion for bulk IG precipitation is quenched; and the wafer Fe concentration for a uniformly doped sample reaches an asymptotic value of 10^{12} cm^{-3}.

Next we explore the effect of initial contamination level on the residual [Fe$_i$] after cooling for an epitaxial wafer with IG sites as described above. Figure 5-5 compares the simulation results for three initial contamination levels: one is saturated at the

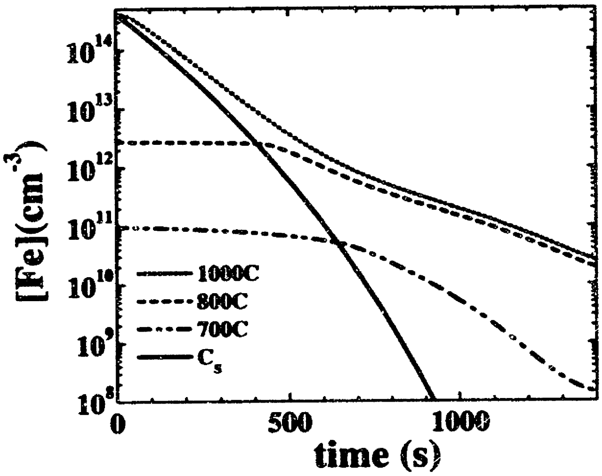

Figure 5-5: Simulation of a cool from 1000°C at 0.5°C/s for Fe contaminated epitaxial wafers of varying initial Fe_i contamination level. N_{IG} is 10^9 cm^{-3}, R_{IG} is 20 nm, and the DZ width is 20 μm.

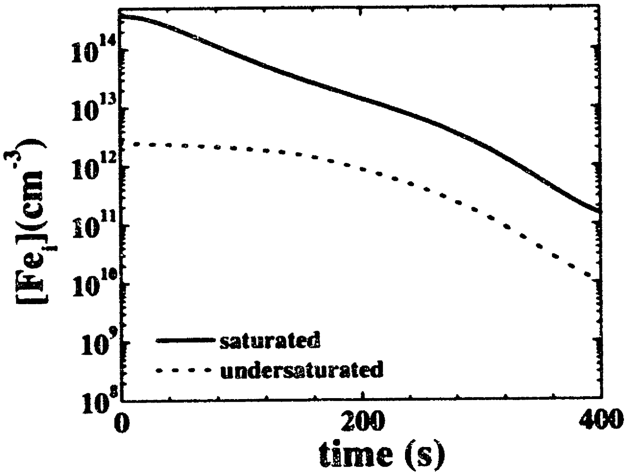

Figure 5-6: Simulation of a cool from 1000°C at 1.67°C/s for Fe contaminated epitaxial wafers of varying initial Fe_i contamination level. N_{IG} is 10^9 cm^{-3}, R_{IG} is 20 nm, and the DZ width is 20 μm.

1000°C initial temperature; the second contains levels of Fe equivalent to the solubility at 800°C, and the third contains levels of Fe equivalent to the solubility at 700°C. The saturated wafer becomes supersaturated upon cooling and gettering is driven by IG precipitation in the substrate. The undersaturated wafers show little gettering until the temperature falls below the solubility limit and IG precipitation reduces the substrate [Fe_i]. The value of k increases as the temperature decreases, but it is still close to unity at 700°C, and negligible gettering occurs. As the temperature continues to drop, we can see that the sample with the lowest level of contamination is able to achieve a much lower residual near surface [Fe_i] content due to less mass transport needing to occur. The more heavily contaminated samples end with roughly equivalent residual contamination levels. If we redo the simulations with a faster cooling rate, Figure 5-6, for the two more heavily contaminated wafers, we see that mass transport limitations cause a separation in the degree of supersaturation between these two cases as well. Clearly k helps increase the gradient at the epi/substrate interface to aid mass transport at lower temperatures, but to make a process completely insensitive to the degree of contamination, an even more patient cooling regime would be required.

We are interested in knowing the design trade-offs on gettering ability of the DZ width. Having too small of a DZ width can cause IG site induced strain effects on the device region in IC manufacturing. We explore shortening the DZ width from 20 μm to 11 μm on gettering effectiveness. Figure 5-7 compares epilayer gettering for these two denuded zone widths, and while there is some difference in near surface residual contamination for the case of the slow cool of 0.5°C/s, it is not significant. For the more aggressive cooling rate of 1.67°C/s and an even larger difference in DZ width, ranging from 20 μm to 5 μm, Figure 5-8 there still is less than an order of magnitude difference in the resulting near surface residual contamination level. The denuded zone width sets the diffusion length for IG precipitation that depletes Fe from the epilayer/substrate segregation interface. The width affects the slope of the gradient of [Fe_i] away from the interface, but not as strongly as other design parameters do.

IG site density and radius are another set of wafer design parameters that can

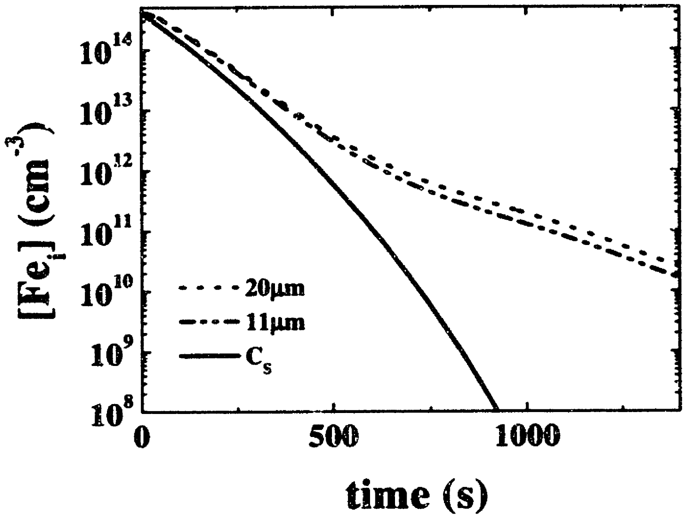

Figure 5-7: Simulation of a cool from 1000°C at 0.5°C/s for Fe contaminated epitaxial wafers of varying denuded zone width. N_{IG} is 10^9 cm^{-3}, R_{IG} is 20 nm, and the initial [Fe$_i$] is equal to C_s at 1000°C.

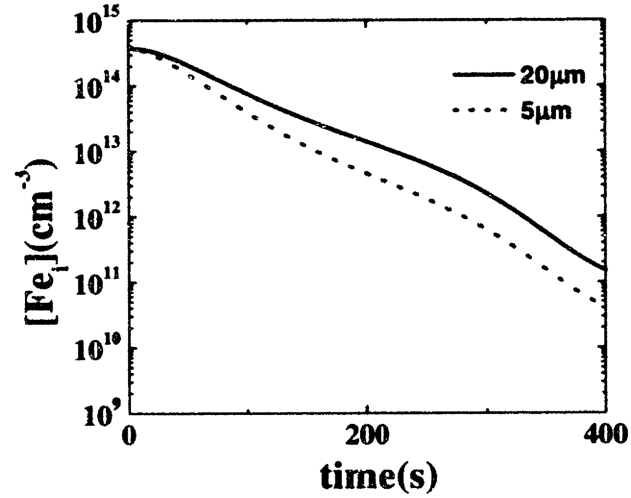

Figure 5-8: Simulation of a cool from 1000°C at 1.67°C/s for Fe contaminated epitaxial wafers of varying denuded zone widths. N_{IG} is 10^9 cm^{-3}, R_{IG} is 20 nm, and the initial [Fe$_i$] is equal to C_s at 1000°C.

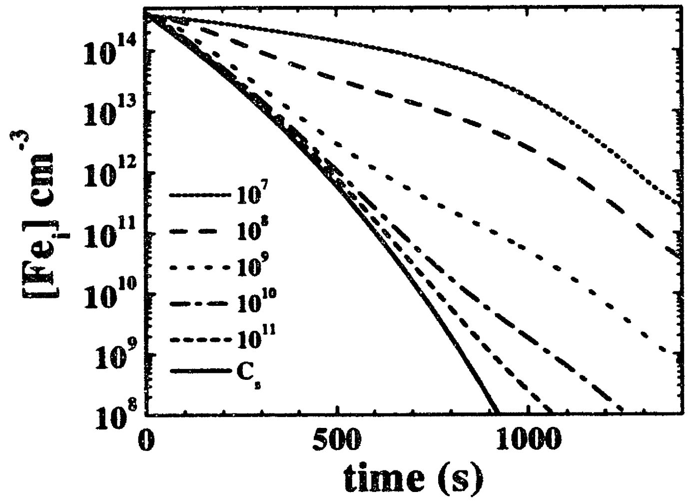

Figure 5-9: Simulation of a cool from 1000°C at 0.5°C/s for Fe contaminated epitaxial wafers of varying N_{IG} and R_{IG} such that IG site volume is held fixed. DZ width is 20 μm and the initial level of [Fe$_i$] equal to C_s at 1000°C.

be controlled within limits. We explore the effect of varying N_{IG} and R_{IG} such that the overall phase fraction of oxide remains fixed. Figure 5-9 displays the results of simulation of role of IG site density in gettering for the slow cool of 0.5 C/s, DZ width of 20 μm and initial contamination level of C_s at 1000° C. The density of IG sites has a marked effect, since it controls the rate of equilibration of the substrate and thereby directly sets the level of one end of the [Fe$_i$] concentration gradient.

5.3 TTT as Process Design Diagram

From looking at the simulation of various wafer designs with different cooling rates, we begin to see the way that time and temperature interact with the wafer design and the initial contamination level to create a particular degree of gettering effectiveness. In order to describe the gettering effectiveness of a wafer/process system in as complete and informative a way as possible, we introduce the time-temperature-transformation diagram [36].

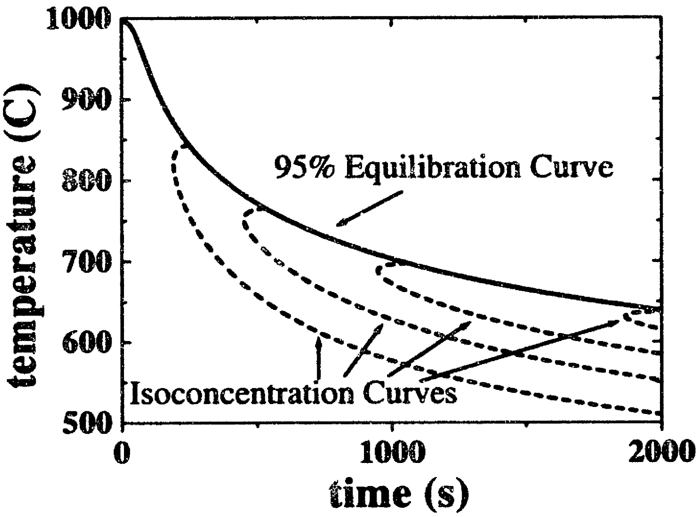

Figure 5-10: Time-Temperature-Transformation curve for isothermal treatment of Fe contaminated Si wafer with uniform light doping and IG sites. The solid line represents the time to reach 95% equilibration at each temperature. Dashed lines are iso-concentration curves, or time to cross the concentration level noted.N_{IG} is 10^9 cm^{-3}, R_{IG} is 20 nm, DZ width is 20 μm and the initial level of $[Fe_i]$ equal to C_s at 1000°C.

The TTT diagram is constructed from the family of isothermal heat treatment curves. The curve that joins the saturation points for each temperature is the curve that gives time to reach equilibrium as a function of temperature. After crossing the equilibration curve in time for a given temperature, there is no change in [Fe] as there is no longer any driving force to remove Fe from the solid solution. In addition to the equilibration curve, iso-concentration curves are included. The iso-concentration curve gives the time to reach a specified final Fe concentration as a function of temperature. This curve is most valuable to estimate if the wafer/process system will meet process specifications.

A calculated TTT diagram is presented in Figure 5-10. For this diagram, we assume an initial Fe contamination level of $4x10^{14}$ cm^{-3} and an IG site density of 10^9 cm^{-3} with radius of $2x10^{-6}$ cm. Diffusion limited kinetics are assumed as shown by the monotonically increasing times to equilibrium with decreasing temperature. The

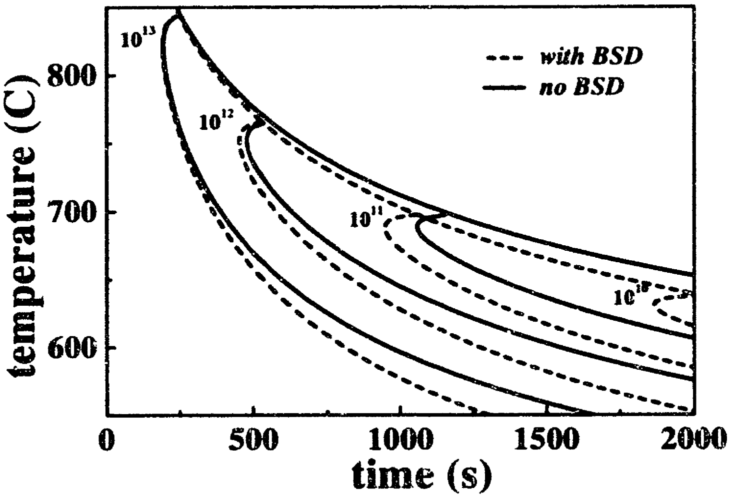

Figure 5-11: Time-Temperature-Transformation curves for isothermal treatment of Fe contaminated Si wafer with IG site only compared with a wafer with both IG sites and BSD. N_{IG} is 10^9 cm^{-3}, R_{IG} is 20 nm, DZ width is 20 μm and the initial level of $[\text{Fe}_i]$ equal to C_s at 1000°C. The BSD is modeled by N_{IG} of 10^{11} cm^{-3} and R_{IG} is 2 nm at the back surface of the wafer.

more typical C-shaped curve represents reduced nucleation rates at higher temperatures. Effective heterogeneous nucleation sites enable the kinetics to be diffusion limited. In contrast, the iso-concentration curves do exhibit a nose shape due to the tradeoff between increased diffusivity at high temperatures and a higher degree of supersaturation to drive precipitation at low temperatures.

In Figure 5-11 we present a comparison of two TTT diagrams, one for the case of no back surface treatment and one with an appreciable density of nucleation sites at the back surface. We model the BSD as a region with a high density of IG precipitation sites to simulate the role grain boundaries and dislocations. N_{IG} was set at 10^{11} cm^{-3} and the effective radius of the IG site was set at 2 nm. The BSD of a wafer will vary depending on how it has been generated, so we treat it as an adjustable parameter within physically reasonable limits. The BSD serves as a sink, but the large diffusion lengths require long times for BSD to produce a significant effect on $[\text{Fe}_i]$ in the epitaxial layer.

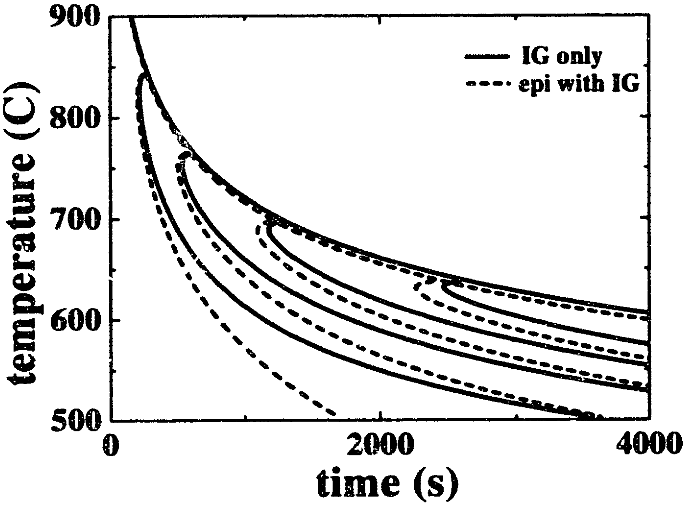

Figure 5-12: Time-Temperature-Transformation curves for isothermal treatment of Fe contaminated Si wafer with IG site only compared to IG sites working in concert with segregation from a lightly doped epitaxial layer. For both wafers, N_{IG} is 10^9 cm^{-3}, R_{IG} is 20 nm, DZ width is 20 μm and the initial level of [Fe$_i$] equal to C_s at 1000°C. For the case of epitaxial wafer, the doping in the substrate is 10^{19} cm^{-3}.

In the temperature range of 700-1000°C, there is not much difference between the curves. For temperatures below 700°C, the impact of BSD in reducing time to reach a particular residual Fe concentration becomes increasingly marked as temperature decreases. At higher temperatures, the gradient due to different equilibration rates in the bulk and back surface region is rapidly eroded because of the relatively high diffusivity. At lower temperatures, the greater degree of supersaturation partially compensates the reduction in diffusivity for the last term in equation 5.1. However, the reduction in D at lower temperature will allow the BSD to generate a gradient that will significantly enhance mass transport from the front of the wafer relative to the no BSD case.

In figure 5-12, we compare the TTT diagrams for a polished, or uniformly doped, wafer and an epitaxial with substrate doping of 10^{19} cm^{-3}. As with the BSD/noBSD comparison, the lower temperature show marked separation between the epi and the polished wafers. The value of k is converging to one at high temperatures, so we expect the differences to vanish at high temperature. The extreme enhancement of k at low temperatures makes the difference much more pronounced than with the case of adding BSD. This gives of a sense of the potential of the segregation gettering mechanism and the BSD gettering mechanism relative to each other.

The TTT diagram provides a means to view all temperature regimes at once. It provides greater insight into the tradeoffs between parameters, and, finally, it allows for fast estimation of how a process regime will determine the gettering capability of a particular wafer design.

Now we extend our simulation to explore other metals. We compare a 0.5°C/s cool with identical IG sites, N_{IG} is 10^9 cm^{-3} and R_{IG} is 20 nm, for four different TM, Fe, Ni, Co and Cu. Cu and Ni have higher solubility limits than Co and Fe, however, Cu, Ni and Co are all faster diffusers than Fe. Even as we saw in figure 5-9 that the DZ limit is dependent on N_{IG} and R_{IG}, for fixed values, we can compare the DZ limits, of gettering freeze-out points, for the different metals. Fe reaches the DZ limit at the highest temperature due to its relatively low diffusivity. This means Fe has less driving force for precipitation at the point it becomes immobile. This is consistent with the fact that Cu, Ni and Co are known to be haze formers, but Fe can only form haze under carefully controlled conditions. Significant precipitate growth requires large undercooling coupled with a high degree of mobility. Cu, Ni, and Co satisfy these requirements and have a much easier time aggregating out of solution.

While Cu, Ni and Co are known to form haze, or near homogeneous precipitates, it is still possible to aggregate these impurities at IG sites due to the reduced barrier to nucleation at these sites. As long as the sites are dense enough and have a reasonable capture radius, as reflected in R_{IG}, the IG can frustrate haze formation. We generate TTT diagrams for Cu (figure 5-14), Ni (figure 5-15) and Co (figure 5-16).

By comparing the TTT diagrams of different metals as in figure 5-17, we can see the effect that solubility and diffusivity have for each metal in gettering. Cu will tolerate the fastest cooling rate and Co, due to its relatively low solubility, will reach the 10^{10} cm^{-3} iso-concentration curve in the shortest time. Overlaying all likely contaminant metals allows simultaneous optimization of the process to getter the all.

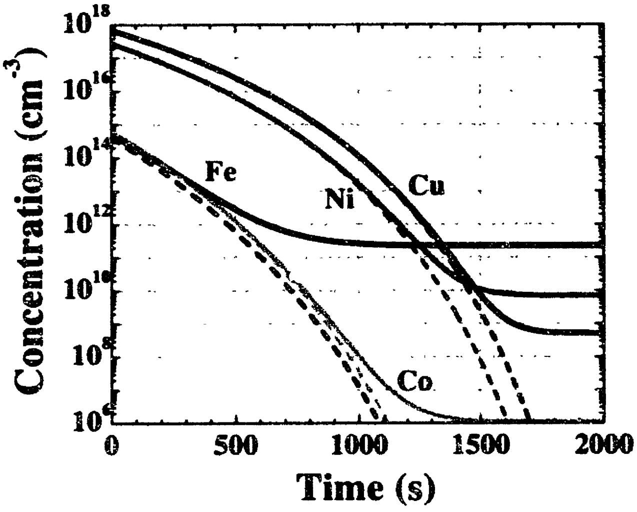

Figure 5-13: Simulation of a cool from 1000°C at .5°C/sec for Cu, Ni, Co and Fe (solid curves) with their respective C_s curves (dashed) as T drops. N_{IG} is 10^9 cm^{-3} and R_{IG} is 20 nm.

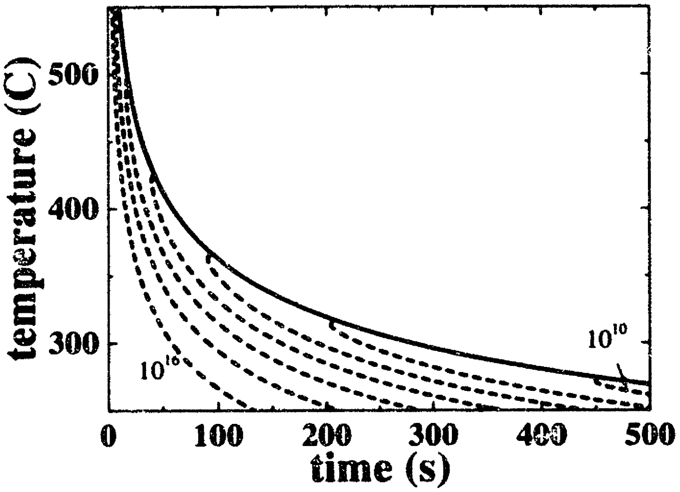

Figure 5-14: Time-Temperature-Transformation curve for isothermal treatment of Cu contaminated Si wafer with IG site. N_{IG} is 10^9 cm^{-3}, R_{IG} is 20 nm. Initial Cu contamination was set equal to C_s at 900°C.

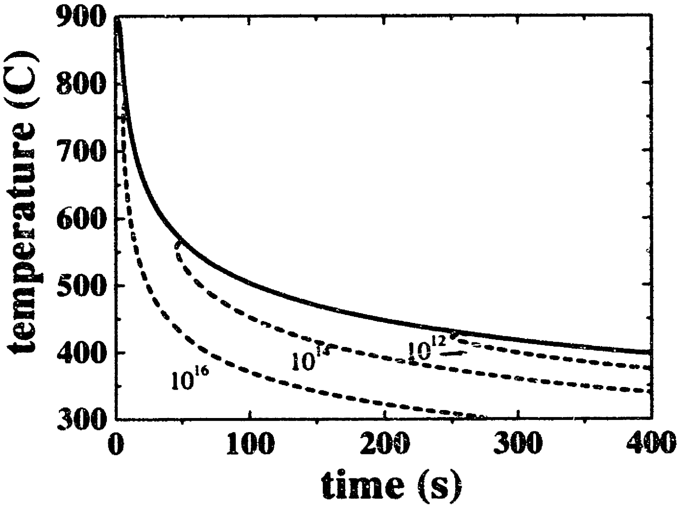

Figure 5-15: Time-Temperature-Transformation curve for isothermal treatment of Ni contaminated Si wafer with IG site. N_{IG} is 10^9 cm^{-3}, R_{IG} is 20 nm. Initial Ni contamination was set equal to C_s at 900°C.

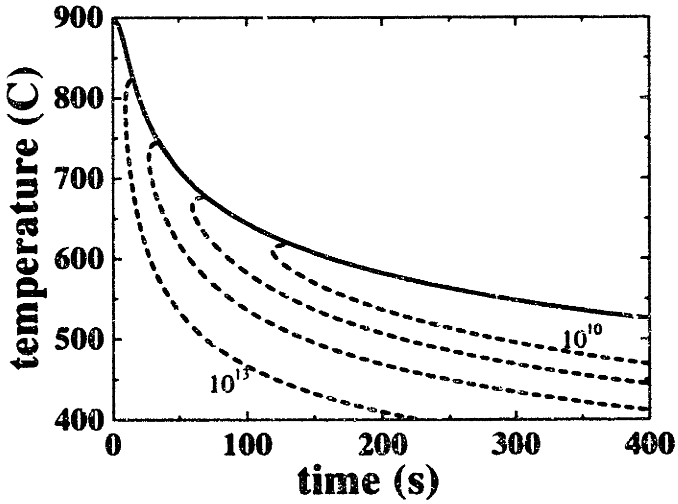

Figure 5-16: Time-Temperature-Transformation curve for isothermal treatment of Co contaminated Si wafer with IG site. N_{IG} is 10^9 cm^{-3} and R_{IG} is 20 nm. Initial Co contamination was set equal to C_s at 900°C.

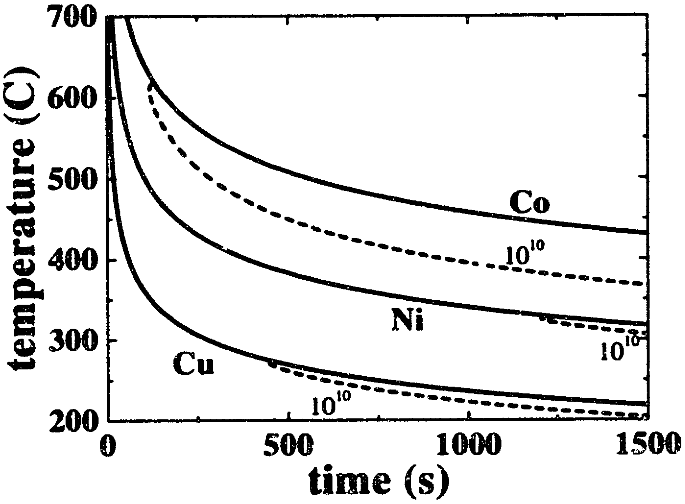

Figure 5-17: Time-Temperature-Transformation curve for isothermal treatment of Cu, Ni and Co contaminated Si wafer with IG gettering mechanism. Included are the 95% equilibration curve and the 10^{10} cm^{-3} iso-concentration curves for each metal. N_{IG} is 10^9 cm^{-3} and R_{IG} is 20 nm for all cases. Initial metal contamination was set equal to C_s at 900°C for each case.

For the case shown here, the high T cool rate would be dictated by the equilibration curve of Co, but the lower T rate (below 450°C would be determined by concern for maximal Ni gettering.

The TTT diagram serves as a design diagram for TM gettering. It can be used to display the kinetic and thermodynamic limits for each metal for a given wafer design, or it can be used to compare wafer parameter trade-offs for one or more metals.

Chapter 6

Gettering Experiments

Experimental gettering studies were carried out with Fe [57, 54, 58] and Cu in various wafer configurations. The experimental procedure, results and analysis are presented in this chapter.

6.1 Fe Gettering Studies

The Fe gettering work involved four main parts. The first was intentional contamination of the p-type Si samples at a high drive-in temperature of 940-980°C. The next was preparation of the surface in one of three configurations before the gettering heat treatment step: a) leaving the $FeSi_2$ formed during the drive-in step in place, b) stripping the $FeSi_2$ and allowing native oxide to form, or c) stripping the $FeSi_2$ and replacing it with high purity evaporated Al. After the surface treatment was in place, the gettering heat treatment step was carried out at temperatures ranging from 700-810°C for varying lengths of time. The last step was Deep Level Transient Spectroscopy (DLTS) measurement of the resulting Fe contamination in each sample by means of the well-known FeB pair defect level.

In order to introduce Fe in a controlled way, we evaporated Fe onto clean, prepared Si surfaces. We cleaved p-type CZ Si wafers with [B] of $1.3x10^{15}cm^{-3}$ and thickness of .06 cm into 1x2 cm pieces and subjected them to a standard organic clean of 5 min. each of trichloroethane, acetone, and methanol in an ultrasonic bath followed by 18 ohm-cm DI water rinse. We then removed the Si surface oxide with a 3 min. etch in HNO_3 and HF in the ratio of 20:1. Before loading the samples into an evaporation chamber for evaporation, the samples were given a last dip in dilute 5% HF to remove any regrown native oxide.

We evaporated 99.9999% pure Fe onto both sides of the Si samples. We then sealed samples individually into evacuated quartz ampoules with pressures in the 10^{-5} torr regime. The ampoules were suspended in a vertical furnace at the drive-in temperature for two hours to insure uniform impurity distribution throughout the sample. The heat treatment was followed by a quench into pump oil at room temperature to freeze in contamination levels of the solubility limit at the drive-in temperature.

We then prepared the sample surfaces for the gettering heat treatment step. Some samples, the $FeSi_2$-contact group, would be re-heated with the $FeSi_2$ surface phase left intact. Others required that the $FeSi_2$ formed during the drive-in stage be stripped by means of a 10:1 mixture of HNO_3 and HF. We left some of these samples, the SiO_2-surface group, as is, we subjected a last set, the Al-contact group, to the standard organic clean, oxide etch and then evaporation of 0.4 μm 99.9999% pure Al on both surfaces.

We put aside one sample of the SiO_2-surface group for each drive-in temperature to serve as controls and individually sealed the remaining samples into evacuated quartz ampoules with a pressure of 10^{-5} torr.

6.1.1 Analysis of Results

In the preceding chapters, we have described the various components needed to simulate gettering of Fe.

One final aspect that needs to be included in simulation of the Fe-gettered samples described in this chapter is the generation of the appropriate time-temperature curve for the samples as they equilibrate to the furnace temperature. Since the samples have been sealed in evacuated quartz ampoules, we estimate that the dominant mechanism for heating will be radiative. Radiative heating tends to be rapid for an object with a high surface to volume ratio. Since $FeSi_2$ and SiO_2 have low coefficients of reflection, the samples with these surface treatments should equilibrate to the furnace temperature quite rapidly. Because molten Al is highly reflective, the samples from the Al-contact group will demonstrate significant thermal lag. In order to compare samples with these different surface treatments, we generate the radiative heating curves, T(t), for the three different reflectivities. We make use of the radiative heat transport equation:

$$\frac{\partial T(t)}{\partial t} = \frac{A}{V\rho C_p}\varepsilon\sigma\left(T_f^4 - T(t)^4\right) \tag{6.1}$$

here A and V are the sample area and volume respectively, ρ is the sample density, C_p is the heat capacity, and T_f is the furnace temperature. The emissivity, ε, of the sample surface, is the fraction of emitted energy from a particular surface relative to the energy emitted from a black-body at the same temperature, and σ is a constant from the *Stefan-Boltzmann* equation and is given by:

$$\sigma = \frac{2\pi^5 k_B^4}{15c^2h^3} = 5.669x10^{-8}W/m^2K^4 \tag{6.2}$$

where c is the velocity of light and h is Planck's constant. The solution to equation 6.1 is transcendental, but T(t) curves can be easily generated numerically. Figure 6-1 contains T(t) curves for the Si samples subjected to radiative heating for a range of ε values representing different surface treatments. While ε values for materials are often not available or highly sensitive to the material surface condition, we see from the heating curves that samples with surfaces having ε values between 0.4-0.8 will experience negligible thermal lag for the time scales considered in these gettering studies ($\geq$ 500s.) The Al-contact samples, however, will have ε at least as low as that for highly polished solid Al, 0.05, making heating time non-negligible for these samples. The thin surface layers will not have a significant impact on the thermal mass or the C_p of the samples and conduction throughout the sample is assumed to be rapid compared to the radiative heating time.

While data for the emissivity of molten Al is not available, we predict that it

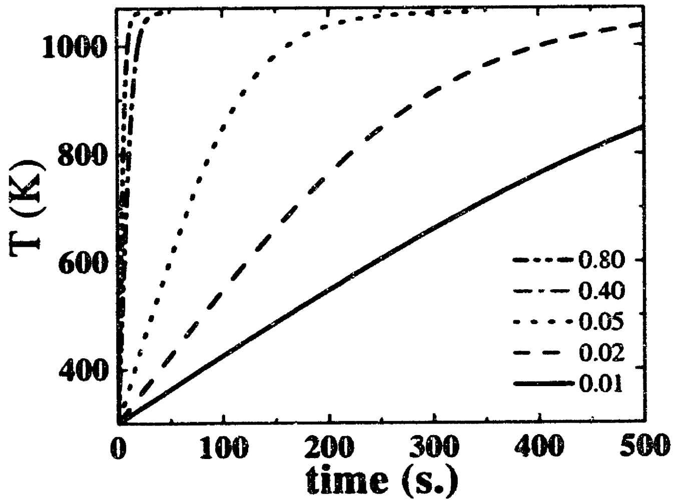

Figure 6-1: Radiative heating curves to reach T_f for various ε values.

should be as low or lower than the case for highly polished Al due to the lack of an oxide layer with its degree of anti-reflection effect.

We present in figure 6-2 data from Nakishima, *et al.* [57] for gettering treatments done on samples with $FeSi_2$ and Al contacts. The curve $FeSi_2$ represents simulations performed with the assumption of the surface concentration being fixed at the C_s for Fe at the gettering treatment temperature and fit the remaining decay by adjusting the $N_{IG}R_{IG}$ product in τ_{IG} from equation 4.2. The net rate is given by the following combined exponential decay time constant:

$$\frac{1}{\tau_{tot}} = \frac{1}{\tau_{out}} + \frac{1}{\tau_{IG}} \tag{6.3}$$

The fact that the $FeSi_2$ data is fit exceptionally well by a single exponential decay curve gives us confidence that the same gettering mechanisisms are dominant throughout the gettering treatment.

We then use the τ_{IG} from the $FeSi_2$ fit and simulate gettering of the Al coated samples under the same treatment conditions. For the case of ε set to 0.01, we display Al gettering simulations with a range of constraints on the interface outdiffusion flux, ranging from full outdiffusion flux, F_{out} to flux reduced by a factor of 10^9, $F_{out}/10^9$ to demonstrate the impact a barrier to diffusion at the interface would have on the overall gettering effect. In the case with full F_{out}, we see that the simulation predicts the outdiffusion mechanism will exceed the $FeSi_2$ precipitate dissolution rate, dropping the concentration in the matrix below the solubility limit for Fe in contact with only $FeSi_2$.

The simulations shown in 6-2 show the transition from silicide dissolution limited gettering to gettering rate limited by outdiffusion to the Al layer. The segregation coefficient to the Al layer as calculated in section 3.2 is extremely large, creating a tremendous driving force for outdiffusion to the Al layer. The simultaneous initial $[Fe_i]$ removal from solution to IG sites competes with the outdiffusion gettering mechanism. After a time, the bulk is no longer supersaturated and the IG sites begin to dissolve. If the outdiffusion rate exceeds the dissolution rate, then mass transport will be dissolution rate limited and the $[Fe_i]$ will remain at a fixed value until dissolution is complete. For the simulations where outdiffusion was the full value, F_{out} was estimated from equation 3.26 with D_{int} set at $2D_{eff}$. We then reduced F_{out} by various factors to explore the impact it had on the overall gettering rate. We see that between reduction by a factor of 10^5 and 10^7, the kinetics are sensitive to the outdiffusion rate. Higher outdiffusion flux will make precipitate dissolution the rate limiting step. Slower out difusion will require additional precipitate formation at IG sites.

In figure 6-3, we display the Nakishima gettering data with Al simulation, assuming full interface flux, for a range of emissivity values. These simulations demonstrate that the effects of reduced heating rate and reduced outdiffusion flux are not enough to capture the reduced gettering rate of the Al contact sample group. This gives strong evidence that a growth retardation due to excess I as has been found in the case of SiO_2 is in effect. In addition, the Al data, unlike the $FeSi_2$ contact group data, cannot be fit with a single exponential decay, demonstrating that the rate limiting step for one of the gettering mechanisms is changing over the course of the gettering treatment.

Next we discuss how these findings compare with the data produced by Ahn *et*

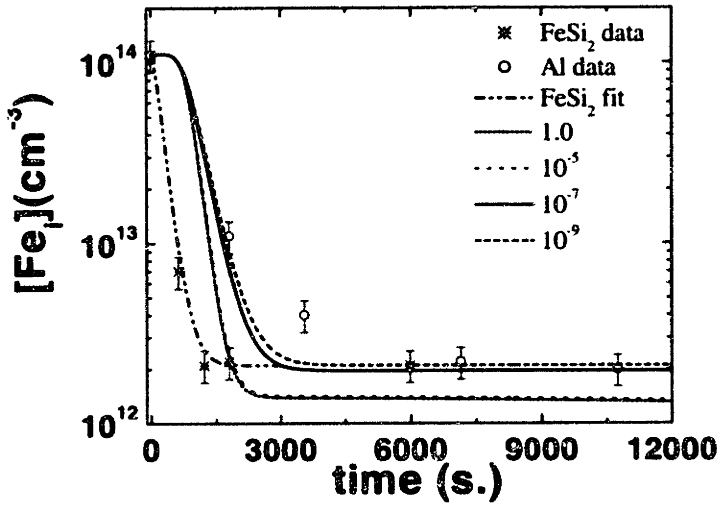

Figure 6-2: DLTS data of Al-contact and FeSi$_2$ case for indiffusion at 940° and heat treated at 790° [57]. Overlayed are simulation curves with ε value of 0.01 and flux into the Al, F_{out}, varying over several orders of magnitude.

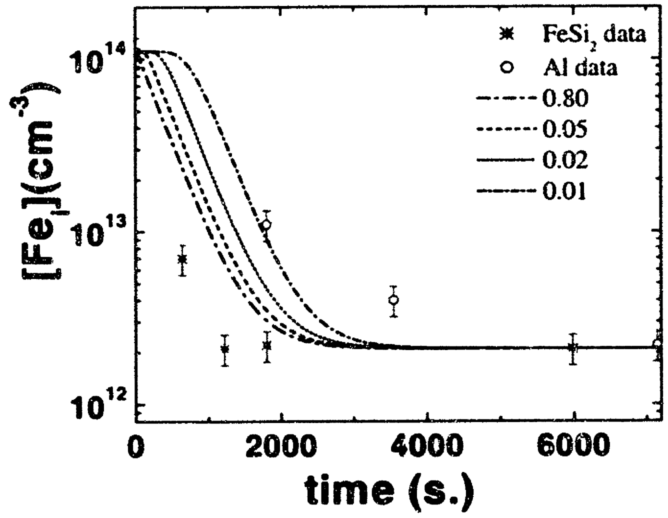

Figure 6-3: DLTS data of Al-contact and FeSi$_2$ case for in-diffusion at 940° and heat treated at 790° [57]. Overlayed are simulation curves for reflecting boundary conditions with ε values ranging from 0.8 to 0.1.

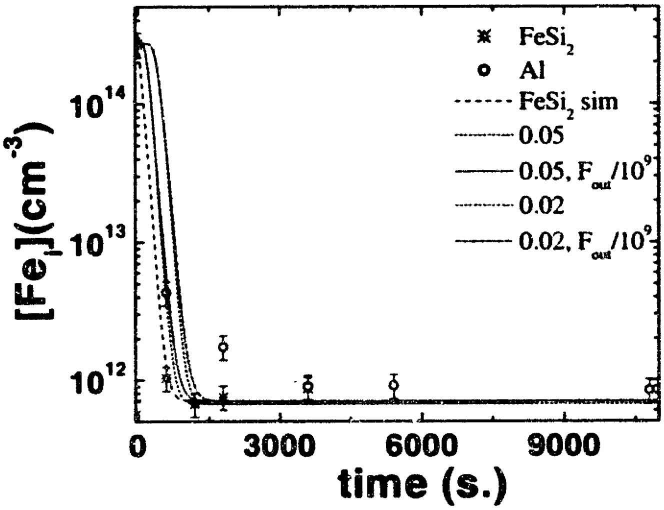

Figure 6-4: DLTS data of Al-contact and $FeSi_2$ samples after Fe in-diffusion at 980° and heat treated at 750° [58]. Overlayed are simulation curves of $FeSi_2$ contacts and Al contacts for two different values of ε, 0.05 and 0.02. The Al ε simulations are each represented by the extremes of interface flux, from full F_{out} to $F_{out}/10^9$.

al. for the three gettering temperatures studied. We present the results of $FeSi_2$ contact and Al contact samples with simulations in figure 6-4 and on an expanded scale in figure 6-5 A simulation with the same assumptions as in the previous case, outdiffusion to the surface concentration of C_s and fitting $N_{IG}R_{IG}$ to determine τ_{IG}. Again, the $FeSi_2$ can be fit exceptionally well by a single exponential decay. We also present simulations of Al contact gettering for two emissivity cases, ε of 0.05 and 0.01, and for the extremes in surface outdiffusion flux. The best fit to the first data point is given by ε of 0.05. We see, just as in case of the Nakishima data, that the Al data does not follow a fixed exponential decay throughout the course of the gettering treatment. This bolsters the hypothesis of growth retardation due to V accumulation.

Figure 6-6 contains post Al gettering DLTS data for treatment at 810°C. Using the same τ_{IG} determined from the 755°C data, we present simulation results for ε of 0.05 and 0.02 with the full surface F_{out} and that of $F_{out}/10^9$. There is not enough data to say whether a simple exponential decay is appropriate or not, but the simulation

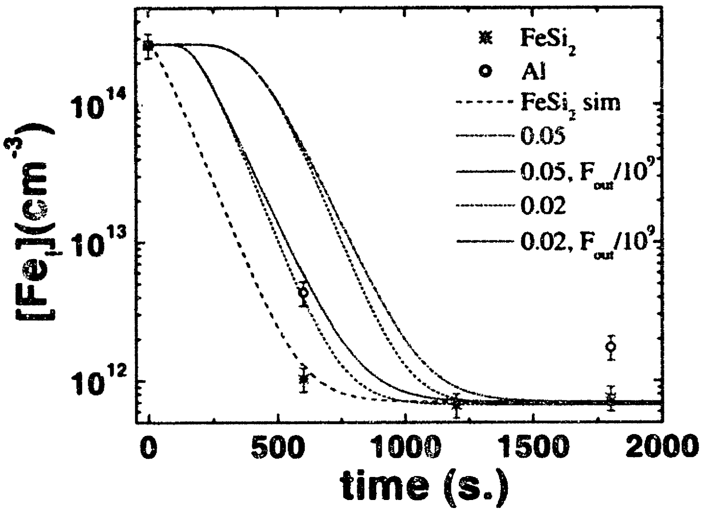

Figure 6-5: DLTS data of Al-contact and $FeSi_2$ samples after Fe in-diffusion at 980° and heat treated at 755° [58]. Overlayed are simulation curves of $FeSi_2$ contacts and Al contacts for two different values of ε, 0.05 and 0.02. The Al ε simulations are each represented by the extremes of interface flux, from full F_{out} to $F_{out}/10^9$. The scale is expanded relative to figure 6-4 to reveal detail.

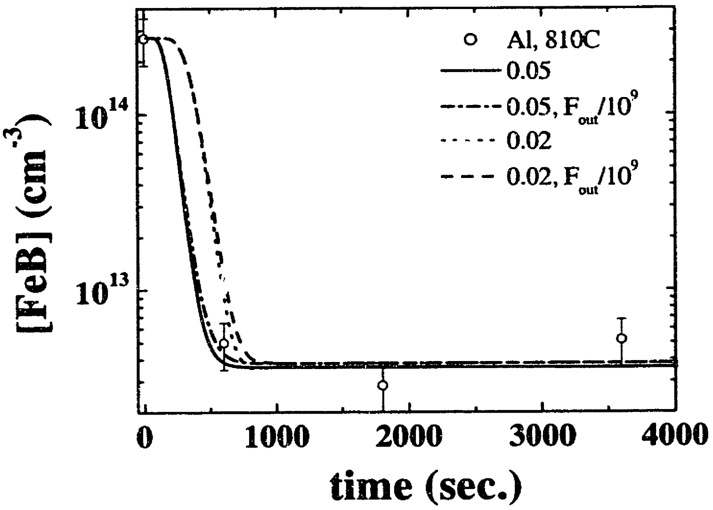

Figure 6-6: DLTS data of Al-contact for in-diffusion at 980° and heat treated at 810° [58]. Overlayed are simulation curves of Al contacts for two different values of ε, 0.05 and 0.02. The Al ε simulations are each represented by the extremes of interface flux, from full F_{out} to $F_{out}/10^9$.

agrees well with the data. For the best fit parameters to the 755°C data of τ_{IG} from the $FeSi_2$ contact samples and ε from the Al contact data, the Al gettering data for 810° is predicted.

Figure 6-7 contains Al contain gettering data for treatment at 695°C. Once again we τ_{IG} from the 755°C data, and simulate Al gettering for ε of 0.05 with the full surface F_{out} and that of $F_{out}/10^9$. Figure 6-8 shows the same data on an expanded scale. There is enough data to show that the [Fe_i] decay is not a single exponential. The simulation cannot capture the mechanism that retards gettering and the concentration decay is not well modeled by a single time constant.

Considering the entire set of data by Ahn *et al.* [58], we see that the retardation of gettering is virtually absent for the 810°C treatment case, apparent in the 755°C treatment case and most significant in the 695°C treatment case. This is consistent with the expectation of a Δg_s increase for the $FeSi_2$ phase due to the accumulation of V. For the least supersaturated case with the highest diffusivity of V, the effect

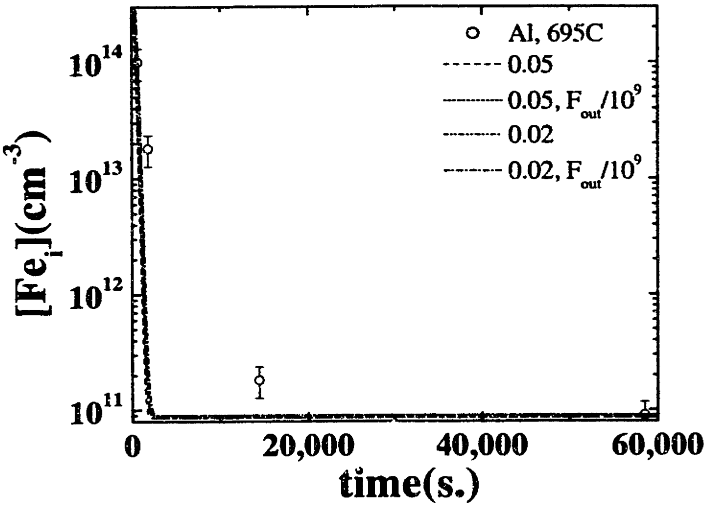

Figure 6-7: DLTS data of Al-contact for indiffusion at 980° and heat treated at 695° [58]. Overlayed are simulation curves of Al contacts for two different ε, 0.05 and 0.02. The Al ε simulations are each represented by the extremes of interface flux, from full F_{out} to $F_{out}/10^9$.

is negligible. For the most heavily supersaturated case, the amount of $FeSi_2$ to be accommodated is the greatest and D_V has its lowest relative value due to the lower temperature. And while the simulation requires parameters for τ_{IG} and ε, τ_{IG} was determined independently from the Al data sets and the best fit for ε was determined from the 755°C Al contact case. The 810°C Al data agrees well with the simulation based on these parameters. The data of the 695°C Al data is not well captured by the simulation. Furthermore, what is it about the Al contact that makes those samples more prone to this effect relative to the $FeSi_2$ samples other than the emissivity effect already discussed and accounted for? We can draw on one additional set of measurements taken from the 755°C data set at positions other than the center of the wafer reveal profiles that qualitatively match those of Al outdiffusion. These data rule out the possibility that outdiffusion is less than $F_{out}/10^7$ such that the rate of Fe_i redistribution across the wafer thickness is negligible compared to the outdiffusion rate. Since the curves occur in the regime beyond that which is well described by our

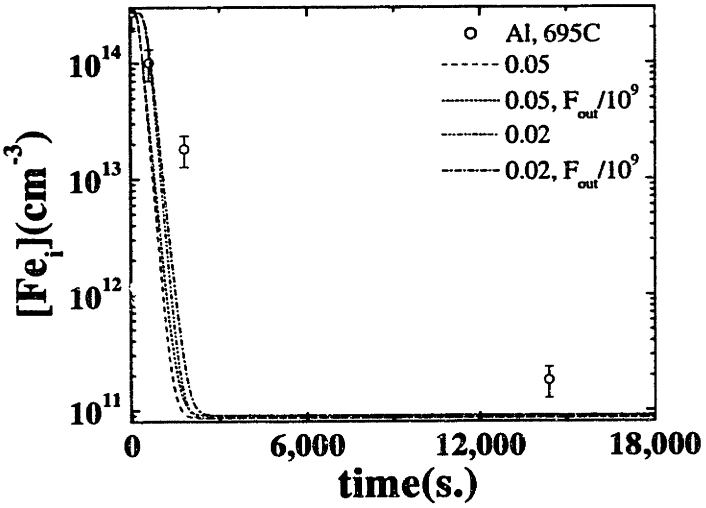

Figure 6-8: DLTS data of Al-contact for indiffusion at 980° and heat treated at 695° [58]. Overlayed are simulation curves of Al contacts for two different ε, 0.05 and 0.02. The Al ε simulations are each represented by the extremes of interface flux, from full F_{out} to $F_{out}/10^9$.

model, it is hard to quantitatively determine much more with certainty from these profiles. Nevertheless, we simulate the change in precipitate volume as a function of outdiffusion flux and present that along with the simulation of volume of precipitate formation for the $FeSi_2$ in figure 6-9. As F_{out} is reduced, more precipitate volume is created in the bulk. If some degree of a barrier to outdiffusion exists, it would explain why more excess V would be generated in Al coated samples relative to $FeSi_2$ ones.

We simulate gettering treatments with $FeSi_2$ and Al contacts and compare with data at various temperatures. The gettering data for $FeSi_2$ contacts follow a simple exponential decay and can be simulated with appropriate choice of τ_{IG}. We recognize that radiative heating dominates the temperature ramp for samples in evacuated quartz ampoules and use reasonable parameters to include this effect in our simulations. The Al contact samples show initial decay that in some cases matches the $FeSi_2$ gettering rate. At longer gettering times for all but the highest gettering treatment temperature, the gettering rate for Al coated samples declines. We propose a pre-

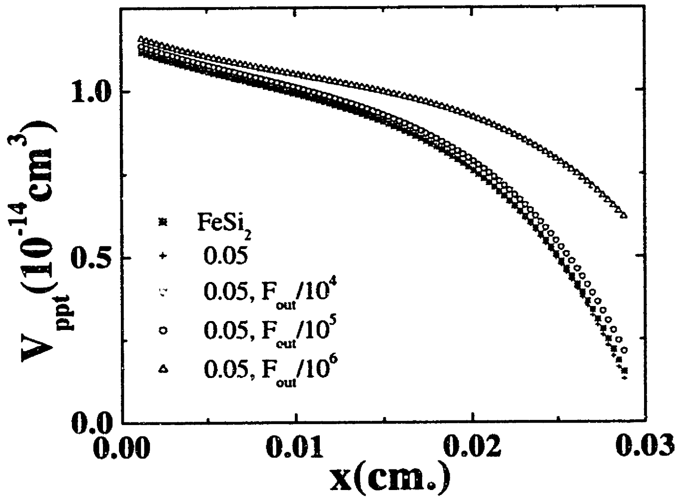

Figure 6-9: Precipitate volume formed at one IG site as a function of wafer position for $FeSi_2$ contact and Al contact with a range of outdiffusion fluxes.

cipitate growth retardation mechanism based on supersaturation of V reducing the ability of precipitates to release Δg_s by emission of V to explain these observations.

Specific volume is defined as the volume per Si atom in the phase [61]. Since $FeSi_2$ is known to have a specific volume below that of Si [62]. It will need to emit V to reduce strain. A metal rich silicide such as Cu_3Si is known to have a higher specific volume per Si [62], and therefor will need to emit I to relieve strain as the silicide precipitates grow.

6.2 Cu Gettering Studies

We have completed Cu gettering experiments in epitaxial p/p$^+$ wafers that were grown and subjected to an IG site formation processes by Komatsu Corp. The epilayers have a resistivity of 11 Ωcm with substrate resistivity of 5 mΩcm. Internal gettering (IG) sites have been intentionally created with a High-Low-High treatment and we have introduced Cu by evaporation at the backside followed by drive in at 950°C for 20 minutes and an oil quench. FZ Si samples of resistivities 15Ωcm and 1100Ωcm respectively were subjected to a similar contamination and heat treatment at either 950°C or 450°C to saturation followed by an oil quench.

The nature of the radiative Cu complex in Si that gives rise to the 1.014 eV no-phonon line in photoluminescence spectroscopy (Pl) has been thought to be related to a Cu-Cu pair [63, 4]. More recently, reserachers believe the radiative center is lineraly proportional to [Cu] and therefore a complex that contains only one Cu atom [64, 65, 66]. In either case, it is firmly established as a signature for Cu contamination. In Pl, various defect centers serve as recombination paths for bound exitons. As doping increases, the dopant sites will play more of a role in dominating recombination, reducing the signal due to other centers. When the doping level is high enough, no Cu line can be seen.

Our PL studies demonstrated that the 1.014eV Cu related line could be observed for the case of the 15Ωcm FZ wafer in-diffused at 450°C and for both the 15Ωcm and the 1100Ωcm FZ samples in-diffused at 950°C. The spectra from samples of both resistivities are shown in figure 6-10. The greater strength of the Cu signal from the more havily doped sample exceeds variation in the system, demonstrating Cu solubility enhancement due to p-type doping. The fact that no Cu related line was observed in the epitaxial layer of the epiwafer in-diffused at 950°C, while the uniformly doped wafer of roughly the same resistivity did, demonstrates that Cu is being gettered from the epitaxial layer towards the subsrate.

We performed a step etch on the epitaxial wafers that had been in-diffused at 950°C to reveal different positions in the epilayers as well as layers within the substrate region. PL on all depths within the epilayers revealed no Cu related line. In addition, haze was observed only at depths below the epilayer/substrate interface in contrast to the uniformly doped wafer case where haze is observed near the surface. Figure 6-11 shows schematically the wafer and step configurations. This indicates a strong gettering effect of the heavily doped substrate on Cu in the epilayer region during the quench. Since Cu has the ability to homogeneously nucleate without intentionally created IG sites, it is essential to understand the kinetics of the near interface haze in order to accurately simulate Cu gettering. Nevertheless, our current under-

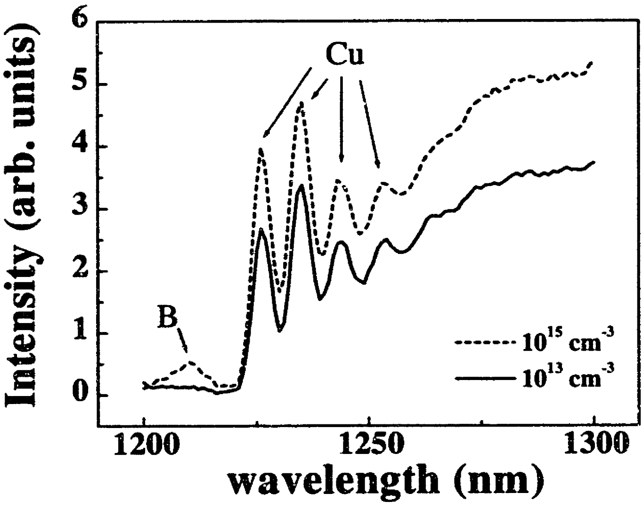

Figure 6-10: Pl data for samples containing Cu with varying degree of p-type doing.

standing allows us to conclude significant Cu mass transport from the epilayer to the heavily doped substrate must have occurred to make the region of appreciable nucleation and growth of silicide precipitates shift away from the surface to beyond the epilayer/substrate interface. A schematic representation is given in figure 6-12. The highest nucleation rate will occurr at the point where the degree of supersaturation is greatest.

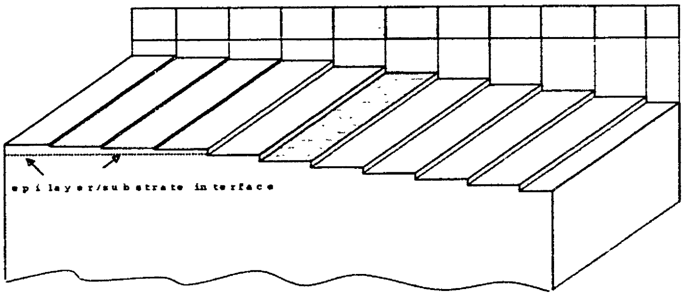

Figure 6-11: Schematic of the haze revealed after step-etching through the epitaxial layer.

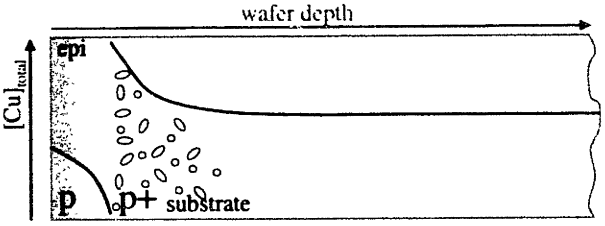

Figure 6-12: Schematic of the expected profile of Cu after high temperature in-diffusion followed by a quench. Homogeneous silicide formation occurs in the heavily doped substrate near the interface with the epilayer.

Chapter 7

Concluding Remarks

7.1 Summary of Achievements

7.1.1 High T Si Data

The commonly used $T^{3/2}$, N_c, N_v model is not accurate for Si, even in the device operation regime, and the available experimentally determined relations of Green do not extend past 500K. We have constructed a DOS model using *ab initio* calculations, temperature appropriate Fermi-Dirac statistics and rigid shift of $E_g(T)$ to generate an alternative method for estimating E_F in the processing temperature regime. Nevertheless, much remains to be explored about high temperature effects on the band structure and DOS. The available data of dopant enhanced solubility of Fe in Si can be modeled within error assuming E_T remains at a constant fraction of E_G by either the $T^{3/2}$ model for N_C and N_V or with our *ab initio method* DOS. There is no compelling evidence at this time for the instability of E_T, however more accurate data for the Si DOS and E_G(T) in the processing temperature regime will shed light on the temperature dependence of E_T.

7.1.2 Simulation

We use what is known about TM defect thermodynamic driving forces and kinetic response to make predictive simulation of gettering during solar cell fabrication possible.

We have developed a simulator to explore the impact of various device and process parameters on gettering effectiveness. The relevant heat treatments are ramps up in temperature, isothermal annealing, and cools from high temperature down to room temperature. We explore a range of surface conditions, density and size of heterogeneous nucleation sites in the bulk, and the degree of contamination in order to create a framework in which to examine these mechanisms acting in concert and to enable process optimization for gettering. We define a parameter called the DZ limit that gives the freeze out point of kinetics during cooling. The DZ limit depends on N_{IC}, cooling rate and TM concentration and delineates the point at which the IG gettering dominated regime ends during cooling. For solar cell processing, segregation to an Al back contact layer is routine. We have estimated the segregation coefficient between a p-type Si wafer and a molten Al layer by the CALPHAPD method and use these results to estimate the thermodynamic driving force for redistribution of Fe into the Al layer.

7.1.3 Process Design TTT diagram

Using the simulator, we have generated time-temperature-transformation diagrams, or TTT diagrams, to enable presentation of the effect of the iso-thermal heat treatment for a given set of wafer parameters over a range of times and temperatures. The equilibration curve gives the time to reach the point in gettering where no more driving forces remain. Iso-concentration curves allow demonstration of when, if ever, particular specifications for residual contaminants levels have been achieved at each temperature. The TTT diagram provides an overview of the gettering potential of the particular wafer design. It can be used to compare wafer design strategies, compare gettering effectiveness for various contaminants, and determine an optimal cooling rate for a particular system.

7.1.4 Gettering Experiments and Analysis

We simulate gettering treatments with $FeSi_2$ and Al contacts and compare with data at various temperatures. The gettering data for $FeSi_2$ contacts follow a simple exponential decay and can be simulated with appropriate choice of τ_{IG}. We recognize that radiative heating dominates the temperature ramp for samples in evacuated quartz ampoules and use reasonable parameters to include this effect in our simulations. The Al contact samples show initial decay that in some cases matches the $FeSi_2$ gettering rate. The simulator successfully predicts gettering for Al samples at 810^o based on τ_{IG} and ϵ at 755^oC. At longer gettering times for all but the highest gettering treatment temperature, the gettering rate for Al coated samples declines. We propose a precipitate growth retardation mechanism based on a build up of V near growing precipitates. Until the V can diffuse away, V emission to relax Δg_{strain} is reduced. The suggested V supersaturation driven precipitate growth model is analogous to the case of SiO_2 growth in Si which transforms from an O dominated mechanism to an I dominated mechanism as precipitates grow.

Cu gettering studies were carried out on p/p^+ epitaxial wafers and polished FZ wafers and analyzed with photoluminescence (Pl) spectroscopy and selective etching. Pl revealed that impurity segregation from the lightly doped region to the heavily doped region has occurred. Etching revealed significant density of defects below the epitaxial layer, giving additional confirmation of the segregation effect.

7.2 Future Work

The clear next step to the gettering simulation work is including the role of point defects, such as I, V, and the dynamic role of O and SiO_2 during gettering. Technological engineering of point defect concentrations could be potentially used to suppress internal gettering in favor of external gettering methods, making the active region of the cell more defect free.

Stepping back to a broader view, device simulation has become a routine tool in device fabrication. Process simulation is not far behind. With the reduction in cost of computational time and power and the increase in cost and environmental impact for Si processing, the more simulation can be used as an intelligent guide to experiment and process development, the better. In order to make simulations quantitative and predictive, we need a solid understanding of Si in the process temperature regime. High temperatures bring many complexities to carrier concentrations and dynamics, but the need and desire for this understanding is out there, it is simply a matter of finding the way to deliver.

Appendix A

Thermocalc Procedure

Thermocalc is a software package that implements extrapolations between binary phase diagrams and known ternary phases. We include an isothermal slice of the Al-Fe-Si system at 1000°C from the literature in figure A-1 [42] for comparison to an isothermal slice at the same temperature generated using Thermocalc, figure A-2. Finally, we iclude the data-bases that were generated with the guidance and assistance of Larry Kaufman. Since our interest was in the Fe poor region of the Al-Fe-Si, we suspended several phases in the Fe rich region to achieve convegnce, but this should have no impact on the extremely Fe dilute regions of the ternary.

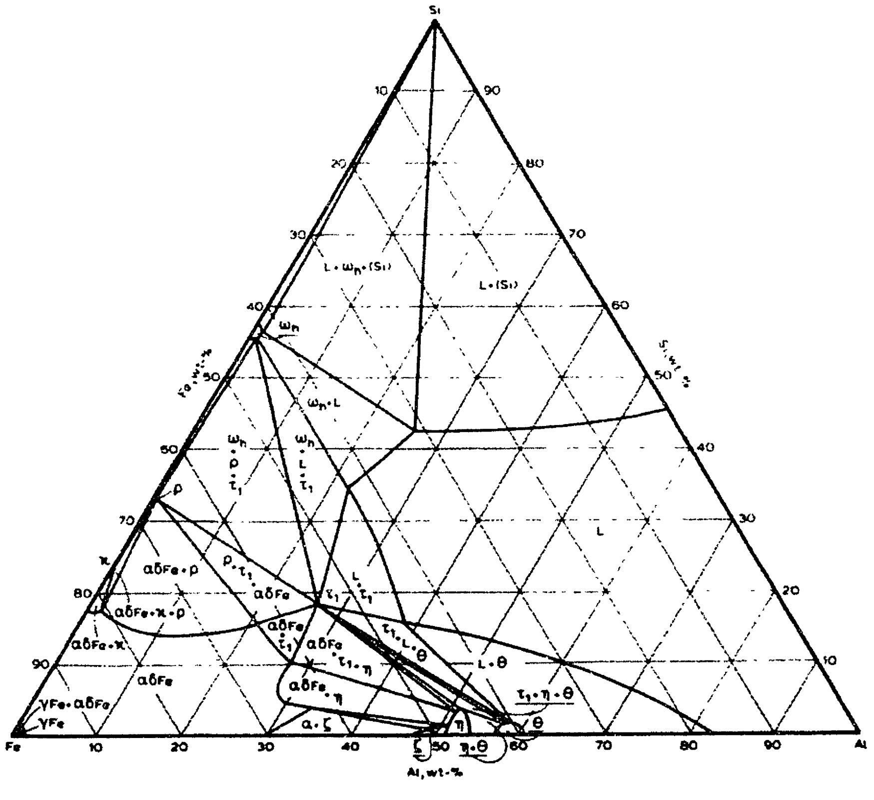

Figure A-1: Isothermal slice of the Al-Fe-Si ternary phase diagram from the literature [42].

Bibliography

[1] Food and Agriculture Organization of the United Nations. State OF Food Insecurtity in the World, 2001. http://www.fao.org/docrep/003/y1500e/y1500e03.htm#P0_0

[2] N. Chomsky. *World Orders Old and New.* Columbia University Press, 1994.

[3] K. Graff. *Metal Impurities in Silicon-Device Fabrication.* Springer Verlag, 1995.

[4] E.R. Weber. *Appl. Phys.*, A 30:1, 1983.

[5] H. Reiss and C. S. Fuller *J. Metals*, 12:276, 1956.

[6] A.L. Smith, S.T. Dunham and L.C. Kimerling. *Physica B*, 273-4:358, 1999.

[7] R.N. Hall and J.H. Racette *J. Appl. Phys.*, 35:379, 1964.

[8] D. Gilles,W. Schröter, and W. Bergholz. *Phys. Rev.*, B 41:5770, 1990.

[9] H. M'saad. *The role of surface and bulk perfection in the processing and performance of crystalline silicon.* PhD dissertation, Massachusetts Institute of Technology, Department of Materials Science, 1994.

[10] J.L. Benton, P.A. Stolk, D.J. Eaglesham, D.C. Jacobson, J.-Y. Cheng, and J.M. Poate. *J. Appl. Phys.*, 80:3275, 1996.

[11] L.L. Chalfoun. *Process Optimization of Alloyed Aluminum Backside Contacts for Silicon Solar Cells.* Master's thesis, Massachusetts Institute of Technology, Department of Materials Science, 1996.

[12] S. Zhao, A.L. Smith, S.H. Ahn, G.J. Norga, M.T. Platero, H. Nakashima, L.V.C. Assali, J. Michel, and L.C. Kimerling. *Materials Science Forum*, 258-2:429, 1997.

[13] S.A. McHugo, R.J. McDonald, A.R. Smith, D.L. Hurley, and E.R. Weber. *Appl. Phys. Lett.*, 73:1424, 1998.

[14] S.M. Sze. *The Physics of Semiconductor Devices.* John Wiley and Sons, 1981.

[15] M.A. Green. *J. Appl. Phys.*, 67:2944, 1990.

[16] F.L. Madarasz, J.E. Lang, and P.M. Hemenger. *J. Appl. Phys.*, 52:4647, 1981.

[17] G. Kresse and J. Furthmuller. *Phys. Rev.*, B 54:11169, 1996.

[18] G. Kresse and J. Furthmuller. *Comp. Mat. Sci.*, 6:15, 1996.

[19] Landolt-Börnstein. *Physics of Group IV Elements and III-V Compounds.* Springer, 1982.

[20] D. Vanderbilt. *Phys. Rev.*, B 41:7892, 1990.

[21] G. Kresse and J. Hafner. *J. Phys: Condens. Matter*, 6:8245, 1994.

[22] D.M. Ceperley and B.J. Alder. *Phys. Rev. Lett.*, 45:566, 1980.

[23] J. P. Perdew and A. Zunger. *Phys. Rev.*, B 23:5048, 1981.

[24] H.J. Monkhorst and J.D. Pack. *Phys. Rev.*, B 13:5188, 1976.

[25] P.E. Blöchl, O. Jepsen and O.K. Anderson. *Phys. Rev.*, B 49:16223, 1994.

[26] Y.P. Varshni. *Physica*, 34:149, 1967.

[27] V. Alex, S. Finkbeiner, and J. Weber. *J. Appl. Phys.*, 79:6943, 1996.

[28] L. Viña, S. Logothetidis, and M. Cardona. *Phys. Rev.*, B 30:1979, 1984.

[29] K.P. O'Donnell and X. Chen. *Appl.Phys. Lett.*, 58:2924, 1991.

[30] R. Pässler. *Solid State Electron.*, 39:1311, 1996.

[31] D. Gilles. *private communication.*, 1998.

[32] W. Shokley and J.L. Moll. *Phys. Rev.*, 119:1480, 1960.

[33] J. DelAlamo. *Integrated Microelectronics Devices: Physics and Modeling.* unpublished text, 1997.

[34] J. Utzig and D. Gilles. In G. Ferenczi, editor, *Materials Science Forum, Vols. 38-41*, Trans. Tech., 1989.

[35] L.C. Kimerling and J.L. Benton. *Physica*, B 116:297, 1990.

[36] A.L. Smith, K. Wada, and L.C. Kimerling. *J. Elec. Soc.*, 147:1154-60, 2000.

[37] L. Kaufman and H. Bernstein. *Computer Calculation of Phase Diagrams.* Academic Press, 1970.

[38] L. Kaufman. *Calphad*, 3(1):45, 1979.

[39] B. Sundman, B. Jansson and J-O. Andersson. *Calphad*, 3(1):153, 1985.

[40] B. Jansson, M. Schalin, M. Selleby and B. Sundman. Eds. C.W. Bale and G.A. Irons. L. Kaufman and H. Bernstein. *Computer Software in Chemical and Extractive Metallurgy.* The Met Soc of CIM, 1993.

[41] T.B. Massalski, J.L. Murray, L.H. Bennett, abd H. Baker, eds.. *Binary Alloy Phase Diagrams, 2nd ed..* American Society of Metals, 1990.

[42] S. Takeda and K. Mutuzaki. *Tetsu-to-Hagané*, 26:335, 1940.

[43] G.H. Vineyard. *J. Phys. Chem. Solids*, 3:121, 1957.

[44] T.E. Seidel, R.L. Meek and A.G. Cullis. *J. Appl. Phys.*, 46:600, 1975.

[45] G.A. Rozgonyi, R.P. Deysher, and C.W. Pearce. *J. Electrochem. Soc.*, 123:1910, 1976.

[46] T.Y. Tan, E.E. Gardner, and W.K. Tice. *Appl. Phys. Lett.*, 30:175, 1977.

[47] S.M. Hu. *Appl. Phys. Lett.*, 31:53, 1977.

[48] B. Leroy, C. Plougonven. *J. Electrochem. Soc.*, 127:961, 1980.

[49] F. Shimura. Eds. F. Shimura. *Oxygen in silicon.* Academic Press, 1994.

[50] S.M. Hu. *Appl. Phys. Lett.*, 36:561, 1980.

[51] D. Gilles, E. Weber, and S. Hahn. *Phys. Rev. Lett.*, 64:196, 1990.

[52] F.S. Ham. *J. Phys. Chem. Solids*, 6:335, 1958.

[53] T.Y. Tan, R. Gafiteanu, and U. Goesele. *Proceedings of the NREL 6th Workshop on the Role of Impurities and Defects in Silicon Device Processing.* Snowmass, Colorado, Aug. 12-14, p.116 1996.

[54] S.H. Ahn, S. Zhao, A.L.Smith, L.L.Chalfoun, H.Nakashima, M.T.Platero, and L.C.Kimerling. *Mater. Res. Soc. Symp. Proc.*. 442: 169, 1997.

[55] D. Gilles, E.R. Weber, and S. Hahn. *Phys. Rev. Lett.*, 64:196, 1990.

[56] D.A. Antoniadis and R. Dutton. *IEEE Trans. Electron. Devices*, ED-26:490, 1990.

[57] S. Zhao. *Defect Reactions and Impurity Control in Silicon.* PhD dissertation, Massachusetts Institute of Technology, Department of Nuclear Engineering, 1997.

[58] S.H. Ahn. *Electrical Studies of Silicon and Low K Dielectric Material.* PhD dissertation, Massachusetts Institute of Technology, Department of Materials Science and Engineering, 1999.

[59] N. W. Ashcroft and N. D. Mermin. *Solid State Physics.* Saunders College Publishing, 1976.

[60] O. Madelung. *Introduction to Solid State Theory.* Springer Verlag, 1978.

[61] M. Ronay and R. G. Schad *Phys. Rev. Lett.* 64:2042, 1990.

[62] P. Villars and L. D. Calvert.

[63] J. Weber, H Bauch and R. Saver *Phys. Rev. B* 25:7688, 1982.

[64] H. B. Ergzraber and K. Schmaly. *J. Appl. Phys.* 78:4066, 1995.

[65] M. Nakamara, S. Ishiwari and A. Tamaka. *Appl. Phys. Lett.* 73:2325, 1998.

[66] M. Nakamara *J. Electrochem. Soc.* 147:796, 2000.

THESIS PROCESSING SLIP

FIXED FIELD: ill. ______ name ______

index ______ biblio ______

► **COPIES:** [✓ Archives] Aero Dewey Barker Hum

Lindgren Music Rotch [✓ Science] Sche-Plough

TITLE VARIES: ► ☐ ______

NAME VARIES: ► ☐ ______

IMPRINT: **(COPYRIGHT)** ______

► **COLLATION:** ______

► **ADD: DEGREE:** ______ ► **DEPT.:** ______

► **ADD: DEGREE:** ______ ► **DEPT.:** ______

SUPERVISORS: ______

NOTES:

cat'r: date:

page: ► J98

► **DEPT:** MatSci.E

► **YEAR:** 2002 ► **DEGREE:** Ph.D.

► **NAME:** SMITH, Aimée Louise